USE OF AN ENGINE CYCLE SIMULATION TO STUDY A BIODIESEL FUELED ENGINE

A Thesis

by

JUNNIAN ZHENG

Submitted to Office of Graduate Studies of
Texas A&M University
in partial fulfillment of the requirements for the degree of

MASTER OF SCIENCE

August 2009

Major Subject: Mechanical Engineering

USE OF AN ENGINE CYCLE SIMULATION TO STUDY A BIODIESEL FUELED ENGINE

A Thesis

by

JUNNIAN ZHENG

Submitted to Office of Graduate Studies of
Texas A&M University
in partial fulfillment of the requirements for the degree of

MASTER OF SCIENCE

Approved by:

Chair of Committee,	Jerald A. Caton
Committee Members,	Timothy J. Jacobs
	Sergio Capareda
Head of Department,	Dennis O' Neal

August 2009

Major Subject: Mechanical Engineering

ABSTRACT

Use of an Engine Cycle Simulation to Study a Biodiesel Fueled Engine. (August 2009)

Junnian Zheng, B.A., Shanghai Jiaotong University

Chair of Advisory Committee: Dr. Jerald A. Caton

Based on the GT-Power software, an engine cycle simulation for a biodiesel fueled direct injection compression ignition engine was developed and used to study its performance and emission characteristics. The major objectives were to establish the engine model for simulation and then apply the model to study the biodiesel fueled engine and compare it to a petroleum-fueled engine.

The engine model was developed corresponding to a 4.5 liter, John Deere 4045 four-cylinder diesel engine. Submodels for flow in intake/exhaust system, fuel injection, fuel vaporization and combustion, cylinder heat transfer, and energy transfer in a turbocharging system were combined with a thermodynamic analysis of the engine to yield instantaneous in-cylinder parameters and overall engine performance and emission characteristics.

At selected engine operating conditions, sensitivities of engine performance and emission on engine load/speed, injection timing, injection pressure, EGR level, and compression ratio were investigated. Variations in cylinder pressure, ignition delay, bsfc, and indicated specific nitrogen dioxide were determined for both a biodiesel fueled engine and a conventional diesel fueled engine. Cylinder pressure and indicated specific nitrogen dioxide for a diesel fueled engine were consistently higher than those for a biodiesel fueled engine, while ignition delay and bsfc had opposite trends. In addition, numerical study focusing on NOx emission were also investigated by using 5 different NO kinetics. Differences in NOx prediction between kinetics ranged from 10% to 65%.

DEDICATION

I want to dedicate this thesis to my parents who give me the greatest support in my life and study.

ACKNOWLEDGEMENTS

I wish to express my deep appreciation to my committee chair, Dr. Jerald A. Caton, for his constant guidance and support throughout this work. I would also like to thank my committee members, Dr. Timothy J. Jacobs and Dr. Sergio Capareda, for their encouragement and support of my thesis work.

Finally, I want to thank everyone in the lab for their continued support and inspiring ideas on my research work.

TABLE OF CONTENTS

Page

LIST OF FIGURES

Page

Page

Page

Page

Page

LIST OF TABLES

1. INTRODUCTION

Compression ignition, direct injection engines (e.g. diesel engine) have dominated the field of heavy-duty vehicles and marine transportations for a long time, and are increasingly being applied in light-duty vehicles in the past 30 years. Compared to the spark ignition engine (e.g. gasoline engine), the diesel engine has considerably higher thermal efficiency due to its lean combustion, with a higher compression ratio, and lack of throttle. However, the major fuel source for diesel engine, the petroleum based fuel, is depleting at a very rapid rate. Of the 102 quadrillion Btu's energy consumed in 2007 in the United States, 39% was from petroleum based fuels and 69% of that was consumed in transportation sector **[1]**. The depletion of petroleum fuel and its increasing cost have raised much interest in looking for the alternate fuel for diesel engines.

Tremendous effort to search for alternative fuels has been made in the past several decades, numerous alternative fuels have been studied and tested, including hydrogen, coal, dimethyl ether (DME), biodiesel, etc. However, due to several certain established end-use requirements, such as availability, supply, safety, cost-efficiency, etc., only a few candidates remain active for testing and research. Major candidates and their main advantages and disadvantages are summarized in table 1 (see next page).

This thesis follows the style of *Journal of Automobile Engineering*.

Table 1 Summary of alternative fuels candidates

Candidates	*Advantages*	*Disadvantages*
Hydrogen	High lower heating value. "Zero" pollutant by emission. Potentially renewable energy source.	Refilling problem. Safety issue due to high pressure tank.
DME	Less PM & NOx emission. High cetane number.	Worse lubrication than diesel. Safety issue due to high pressure tank.
Coal	Large accessible reserve.	Injection problem. Lubrication contamination.
Biodiesel	Low HC and CO emission. Potentially renewable energy source.	Low energy content. Uncertain effect on NOx.

1.1 Biodiesel as an alternative fuel

In the past several decades, it has been found that biodiesel (esters derived from vegetable oils) is a very promising one. The most common blend is a mix of 20% biodiesel and 80% petroleum diesel, called "B20". The widespread use of biodiesel is based on the following advantages **[2]**:

· Biodiesel is potentially renewable and non-petroleum-based

· Biodiesel combustion produce less greenhouse gases

· Biodiesel is less toxic and biodegradable

· Biodiesel can reduce tailpipe emissions of PM, CO, HC, air toxics, etc

· Little modifications are needed for the traditional CI engine to burn biodiesel

Biodiesel also has some negative attributes **[2]**:

· Lower heating value, higher viscosity

· Lower storage stability, material compatibility issue

· Slightly higher NOx emission

Among the above attributes of biodiesel, the higher NOx emissions from biodiesel fueled engines are a major concern due to more and restrict regulations, and therefore it serves as the major motivation of this work.

1.2 Use of the engine cycle simulation to study a biodiesel fueled engine

In modern engine research and study, using hardware experiments alone would be very expensive and time-consuming, and many cause and effect relationships implicit in the test results are often hard to interpret. On the other hand, modeling and simulation approaches, although less precise in predicting the outcome of a specific test, could effectively isolate one variable at a time and conduct parametric studies on it. Therefore simulation could point out cause-effect relationships more clearly, and a validated model could be a very useful tool to study new type of engines or engines running with new type of fuels. Since people still don't have a very clear understanding on the effect of using biodiesel on a diesel engine, together with experimental study, a simulation study of the biodiesel engine is necessary.

Engine cycle simulation models could be divided into three major categories: zero-dimensional models, quasi-dimensional, multi-zone models and multi-dimensional models. Zero-dimensional models have been successfully used to predict engine performance and fuel economy, but they are too simplified to predict the engine emission accurately. On the other hand, though multi-dimensional models could provide the most accurate prediction due to more detailed geometry modeling, the significantly increased computation time becomes a major limiting factor of applying multi-dimensional models. Among them, quasi-dimensional, multi-zone models could be effectively used as an engine development tool because they combine some of the advantages of zero-dimensional and multi-dimensional models. Therefore, quasi-dimensional, multi-zone model would be a good choice for this biodiesel engine study.

2. OBJECTIVES AND MOTIVATIONS

The major objective of this project is to use an engine cycle simulation to study a biodiesel fueled engine focusing on the engine overall performance and emission characteristics. To achieve this objective, several specific tasks need to be done:

1. First of all, by using the engine simulation software *'GT-Power'*, build a biodiesel fueled engine model which is corresponding to the real engine. The model should have submodels which reflect all the features in the real engine, including direct injection, EGR, turbocharging, charged air intercooling, EGR intercooling, and etc. The model would be quasi-dimensional and multi-zonal, and be able to predict engine performance and emissions (e.g. NOx concentration, PM) at different operating conditions.

2. After constructing the model, the second task is to calibrate the model with experimental data at several typical operating conditions (e.g. low speed low load, high speed high load). The major calibration objective is to match the computed pressure diagram and heat release rate diagram with the experimental ones. Before calibration, parametric studies on major adjustable parameters are needed to determine their sensitivity on pressure diagram and other major parameters such as ignition delay, fuel consumption, and etc.. After calibration, the difference between simulation and measurement for main parameters should be lower than 10%.

3. Using the calibrated model, study the effect of various parameters on engine performance and emission for both biodiesel and reference diesel case. By comparing and analyzing the results, look for the cause of changes in performance and emission due to biodiesel combustion in diesel engine.

3. LITERATURE REVIEW

A review of recent biodiesel fueled engine research activities is presented here. Activities can be roughly divided into two aspects: engine experimental studies and numerical studies. Both of these types of studies focus on the performance and emission characteristics of biodiesel fueled engines and comparison to the conventional diesel engine.

3.1 Previous experiment studies

3.1.1 Effect of injection timings

In many papers reviewed, the start of injection(SOI) for biodiesel is advanced than those for conventional diesel engine. As an example, for the experiment done by **[3]**, an earlier start of injection for neat biodiesel fuels was found. The biodiesel fuel injected about 2.3º earlier than diesel no.2, and the B20 (blend of 20% biodiesel and 80% diesel) were 0.25º-0.75º earlier than diesel no.2. According to **[4, 5]**, the SOI are majorly affected by changes in three physical properties: density, bulk modulus of compressibility, and speed of sound. Because of the higher bulk modulus of compressibility and speed of sound for biodiesel, there is a more rapid transfer of the fuel pump pressure wave to the injector needle, resulting in earlier needle lift and effectively a little advance in injection timing. However, this effect only exists in rotary/distributor-style fuel injection pumps, and not in common-rail fuel injection systems.

In terms of NOx emission, advanced injection timing is considered by many authors as a major reason for change in NOx emission for biodiesel engine **[3, 5, 6]**. In the experimental study conducted by **[7]**, tests were done with a Yanmar L70 EE air-cooled, four-stroke, single cylinder DI diesel engine with a maximum power output of 5.8 horsepower, operating at high load and low load. The fuels include BP325 (baseline

petroleum diesel fuel with 325 ppm sulfur), B20, B40, B100, Fischer-Tropsch (FT) diesel and its blend with BP325. The results showed that brake specific NOx emissions decrease with retarded injection timing at all loads. At high load, all the fuels demonstrate roughly the same NOx emissions as a function of fuel injection timing. This observation indicates that for these fuels the engine-out NOx emission differences are related to shifts in SOI timings.

3.1.2 Effect of ignition delay

Most of the studies observed that ignition delay for biodiesel is shorter than that of conventional diesel **[8, 9, 10, 11]**. Eckerle **[8]** did experiments with a Cummins ISB 6.7L six cylinder engine with Bosch CRIN 3.0 HPCR fuel system. In these studies only one of the six cylinders is active and the others are unfired. The study investigated four fuels: Low Cetane Diesel, Low Cetane B20 Blend, High Cetane Diesel, and High Cetane B20 Blend. Results showed that at 1700 rpm low load condition, ignition delay for High and Low Cetane B20 are shorter than High and Low Cetane Diesel, respectively. The difference is 3º for Low Cetane case and 0.5º for High Cetane case.

The decrease of ignition delay varies with different biodiesel feedstock. Some studies **[12]** found that ignition delay of CME (coconut oil methyl ester) is shorter than RME (rapeseed oil methyl ester) but longer than PME (palm oil methyl ester). The decrease of ignition delay also varies with engine operating conditions, i.e. engine speed and load. Experiments done by **[5]** indicated that compared with diesel fuel, ignition delay at 1300 rpm with B20 decreased by 5% at low load and 10% at high load , and at 75% load B20 decreased by 6.9% at load speed and 17.2% at high speed condition. Higher cetane number of biodiesel is generally considered as indication of its shorter ignition delay. Analysis in **[8]** indicated that ignition delay is affected by aromatic hydrocarbon content and is generally characterized by cetane number.

In terms of NOx emissions, ignition delay is also considered by some investigators **[5, 7, 8]** to be an important part of the NOx emission difference between diesel and biodiesel. According to **[8]**, at light load, the relatively longer ignition delay for diesel fuel allow most or all of the fuel to be injected before combustion begins. This pre-mixing results in a more dilute combustion zone and in lower peak combustion temperatures. This in turn results in lower NOx formation in diesel engine compared with biodiesel engine. But **[8]** also indicated that at high load conditions where the combustion is dominated by a diffusion flame, the ignition delay effect is weak and there is only a small net combustion impact associated with burning biodiesel. The difference in NOx between either diesel fuel and its B20 blend is considerably less than the difference in NOx between the two commercial diesel fuels.

3.1.3 Effect of flame temperature and soot radiation

A lot of investigators **[8, 9, 13, 14]** hold that engines fueled with biodiesel have higher flame temperature than conventional diesel engines and the higher flame temperature is one of the major reasons for increased NOx emission from biodiesel engine. Results from **[8]** shows that the higher aromatic content in biodiesel produces higher flame temperatures and therefore higher NOx emissions. The author also indicated that this effect is most significant for modes of combustion dominated by diffusion burning, as is characteristic of higher load engine operation. In addition, the methyl ester compounds in the biodiesel have more double bonds than the base diesel fuel and these double bonds have the effect of increasing the flame temperature **[13]**. From a macroscopic point of view, advanced injection timing and shorter ignition delay produce a higher flame temperature during the diffusion burning period **[9]**. Also, for improved combustion the temperature in the combustion chamber can be expected to be higher **[14]**.

Recent studies have shown that radiative heat transfer from soot could significantly affect the NOx formation during combustion **[15, 16]**. Some investigators have reported that the "cooling effect" of soot radiation may reduce NOx emission by approximately 25% **[15]**. Radiation from soot produced in the flame zone is a major source of heat transfer away from the flame, and can lower bulk flame temperature by 25 K to 125 K, depending on the amount of soot produced at the engine operating conditions. Such reductions in the flame temperature would accordingly decrease the NOx by the thermal mechanism by 12% to 50%. Thus, an in-cylinder soot-NOx tradeoff exists in diesel engines and this tradeoff appears to fit biodiesel emission data well **[13]**. As stated previously, biodiesel fuels in general produce less soot than petroleum diesel fuel, which is likely a consequence of the fuel bound oxygen. This reduction in soot would theoretically reduce the "cooling effect" via soot radiative heat transfer, and thus leave NOx formation unsuppressed. Also, soot radiation may explain the variation in NOx emissions between the different esters of which biodiesel consists **[13]**.

3.2 Previous simulation studies

Due to the subtlety and complexity of comparing biodiesel and diesel combustion in direct injection engines, numerical studies (engine simulations) have been applied in addition to experimental studies.

The numerical study in **[13]** applied a so-called well-mixed balloon model to investigate the flame temperature and NOx formation of biodiesel combustion. Calculation were made using Cantera in a MATLAB environment. The well-mixed balloon is a model that simulates the time history of a jet of fuel into a combustion chamber containing oxidizer. In the well-mixed balloon, the mass output is zero and thus the balloon grows as mass flows in. In time the balloon grows and the fuel-air mixture in the balloon reaches the ignition conditions and then ignites. This leads to a sudden increase in temperature **[13]**. Two fuels, methyl butanoate and methyl trans-2-butenoate,

were simulated, and the results showed that the double bonded methyl trans-2-butaneoate gave a 14 K higher flame temperature than the other fuel. The investigator believed that this change in temperature caused an increase in NOx emissions of 159 ppm **[13]**. Also, the author did the model sensitivity analysis on the influence of the various NOx mechanisms. Results revealed that the thermal NOx mechanism had the most visible contribution to the NOx formation (92%), comparing to other mechanisms such as N_2O mechanism (1%) and Fenimore mechanism (13%) **[13]**.

Due to the over-simplicity of zero-dimensional model, and the long computational time of three-dimensional model, quasi-dimensional multi-zone models are increasingly applied by many investigators **[17, 18, 19, 20]**. The study in **[17]** developed a quasi-dimensional, multi-zone, direct injection (DI) diesel combustion model. The model was implemented in a full cycle simulation of a turbocharged engine. The combustion model accounted for transient fuel spray evolution, fuel-air mixing, ignition, combustion and NO and soot pollutant formation. The results demonstrated that the model can predict the rate of heat release and engine performance with high fidelity, while more effort is needed to enhance the fidelity of emission prediction. Arsie et al. **[18]** reported that the model they developed successfully predicted engine performance and emissions. In addition, the constants in their submodels remained the same throughout the engine operating range, which enabled this quasi-dimensional multi-zone model to be used for prediction purposes. By using the GT-Power software, **[20]** also developed a multi-zone model to analyze the performance and emissions of different types of diesel and biodiesel fuels. The model was calibrated at a default case using normalized burn rate and it was then used to predict pressure diagram, heat release and NOx emissions for soybean based biodiesel, rapeseed based biodiesel and reference diesel. The results showed that three fuels gave almost the same pressure diagram, while the two biodiesel cases gave slightly higher heat release rate than that of diesel case. At two load conditions, results showed 60% higher NOx concentration from the two biodiesels fuel than that of diesel fuel. Since the

model has not been well calibrated at all engine operating conditions, these results could be very preliminary.

To obtain more detailed combustion insight, 3D simulation is still applied by some investigators. In **[8]**, a KIVA model was developed and calibrated using the engine data for diesel no.2 and B100 biodiesel. Good agreement between measured and predicted heat release is obtained with some discrepancies associated with the start of combustion. In terms of emissions, the author compared soot vs. NOx tradeoff between measurement and prediction and the agreement is also quite good. After completing the KIVA model validation, a detailed examination of the impact of engine controls settings on NOx formation due to the lower energy content of the B20 blends was conducted. Two test cycles (UDDS6K and HWY55) were conducted by the KIVA model. Final results showed that at higher speeds and loads, the change in engine control settings due to the lower energy content of the blended fuel led to a NOx increase on the order of 3-4%. The author believed that this accounts for the majority of the NOx difference between a B20 blend and its base diesel fuel.

4. MODELING DI ENGINE IN GT-POWER

4.1 Overview

GT-Power is a popular engine simulation tool which is designed for steady-state and transient simulations. It is applicable to many types of internal combustion engines and provides the user with many components to model any advanced concept.

GT-Power is based on one-dimensional gas dynamics, representing the flow and heat transfer in pipes and other components of an engine system. In addition, many other specialized models (e.g. emission production model, T/C model) can be applied for many kinds of system analysis. The detailed model information related to the present work is described in the following sections.

4.2 Modeling fluid properties

In GT-Power, a gas reference object is commonly described by its C:H:O:N composition, lower heat value, critical temperature and pressure, enthalpy, and transport properties which includes viscosity and thermal conductivity.

For liquids, information about enthalpy, density, and transport properties are the necessary input to GT-Power. In addition, typically every liquid reference object must be associated with a gas reference object so that the properties of the liquid will be known if the fluid evaporates.

The detailed properties of the biodiesel and reference diesel that are used in the simulation is listed in Appendix I.

4.3 Modeling fluid flow in pipes

4.3.1 General governing equations

In GT-Power, the fluid flow in pipes is simplified as a transient, one-dimensional problem, which involves the simultaneous solution of continuity, momentum and energy equations only in flow direction. All quantities are averages across the flow direction since it's a one-dimensional problem.

The whole system is discretized into many volumes, where each flowsplit is represented by a single volume, and every pipe is divided into one or more volumes, see figure 1 **[21]**.

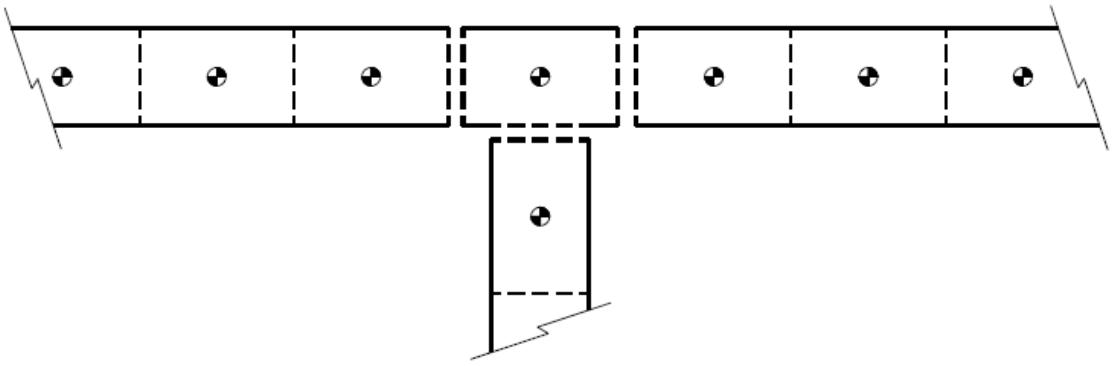

Fig.1 Discretization of pipes in GT-Power

The continuity, momentum and energy equations being solved are **[21]**,

$$\frac{dm}{dt} = \sum_{boundries} \dot{m} \tag{4-1}$$

$$\frac{d(me)}{dt} = p\frac{dV}{dt} + \sum_{boundries} (\dot{m} \qquad (T_{fluid} - T_{wall}) \tag{4-2}$$

$$\frac{d\dot{m}}{dt} \qquad \frac{\sum_{boundries} (\dot{m} \qquad \frac{\rho u|u|}{2} \cdot \frac{dxA}{D} - C_p\left(\frac{1}{2}\rho u|u|\right)A}{dx} \tag{4-3}$$

4.3.2 Friction loss and surface roughness effect

Pressure loss in pipes due to friction is obtained from by several common correlations, using the Reynolds number and the surface roughness.

For smooth surface **[21]**,

$$\begin{cases} C_f = \dfrac{16}{\mathrm{Re}_D} & \text{in laminar region, } \mathrm{Re_D} < 2000 \\ C_f = \dfrac{0.08}{\mathrm{Re}_D^{\,0.25}} & \text{in turbulent region, } \mathrm{Re_D} > 4000 \end{cases} \tag{4-4}$$

For rough surface and turbulent flow **[21]**,

$$C_{f,rough} = \max\left(\frac{0.08}{\mathrm{Re}_D^{\,0.25}}, \frac{0.25}{\left(2\log\left(\frac{D}{2h} \right) + 1.74 \right)^2} \right) \tag{4-5}$$

4.3.3 Heat loss and surface roughness effect

The heat transfer from the fluid to the pipe wall is calculated by correlated heat transfer coefficient. For smooth pipes **[21]**,

$$h_g = \frac{1}{2} C_f \rho U_{eff} C_p \,\mathrm{Pr}^{-2/3} \tag{4-6}$$

For rough surface **[21]**,

$$h_{g,rough} = h_g \left(\frac{C_{f,rough}}{C_f} \right)^n \tag{4-7}$$

where $n = 0.68 \times \mathrm{Pr}^{0.215}$

$h_{g,rough}$ = heat transfer coefficient of rough pipe

$C_{f,rough}$ = friction coefficient of rough pipe

4.4 Modeling cylinder, cylinder valves and ports

To model the cylinder geometry, the bore, stroke, connecting rod length, wrist pin to crank offset, compression ratio, and TDC clearance height are inputted into the program, as shown in figure 2 **[21]**. The detailed values for the cylinder geometry are consistent with the engine specifications from the engine manufacturer. The one exception was the compression ratio which was determined from manual measurement of the clearance volume and the displacement volume. Values used in the simulation are listed in the engine specifications which is described in the next section.

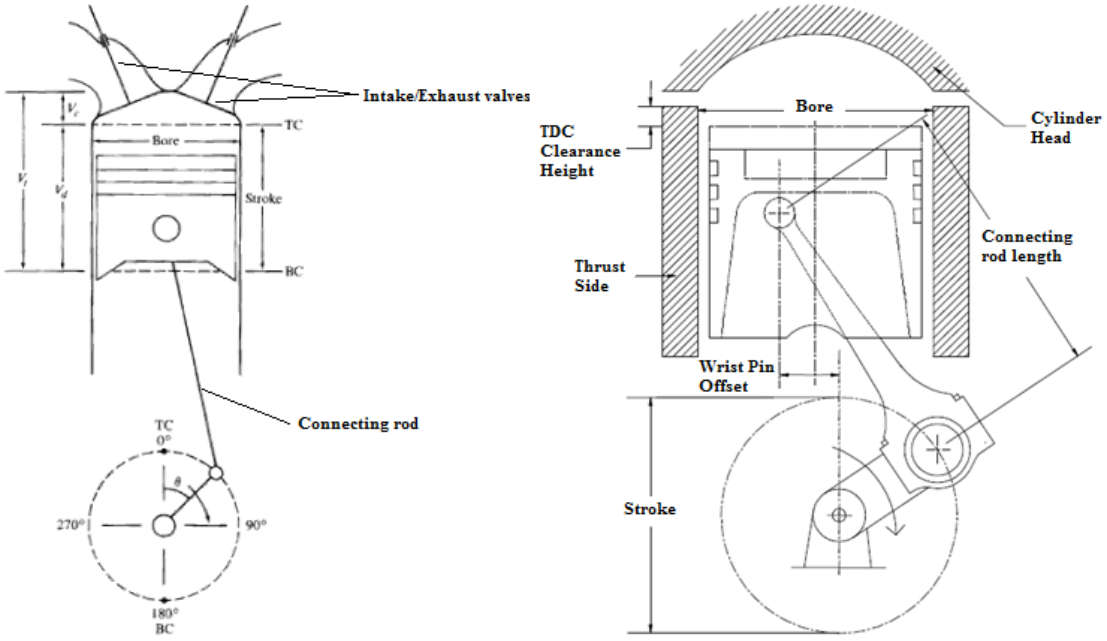

Fig.2 Engine cylinder modeling **[21]**

For valves, the simulation uses a valve lift profile, nominal flow area, and discharge coefficient to describe the cylinder valves. The flow rate is calculated by the following equations **[21]**:

$$\dot{m} \qquad U_{is} = C_D A_R \rho_0 \left(P_r\right)^{1/\gamma} U_{is} \tag{4-8}$$

In the equation, C_D refers to the discharge coefficient which is provided by the

engine manufacturer, and A_R refers to the reference area of the cylinder valves, which is calculated by the relation:

$$A_R = \pi D_{ref} L \tag{4-9}$$

where D_{ref} is the reference diameter of the valve and L is the valve lift for a certain valve lift position. A_R and C_D are unique for each lift position. Figure 3 shows the intake/exhaust valve lift profile, and the detailed discharge coefficients with valve lift can be found in Appendix II.

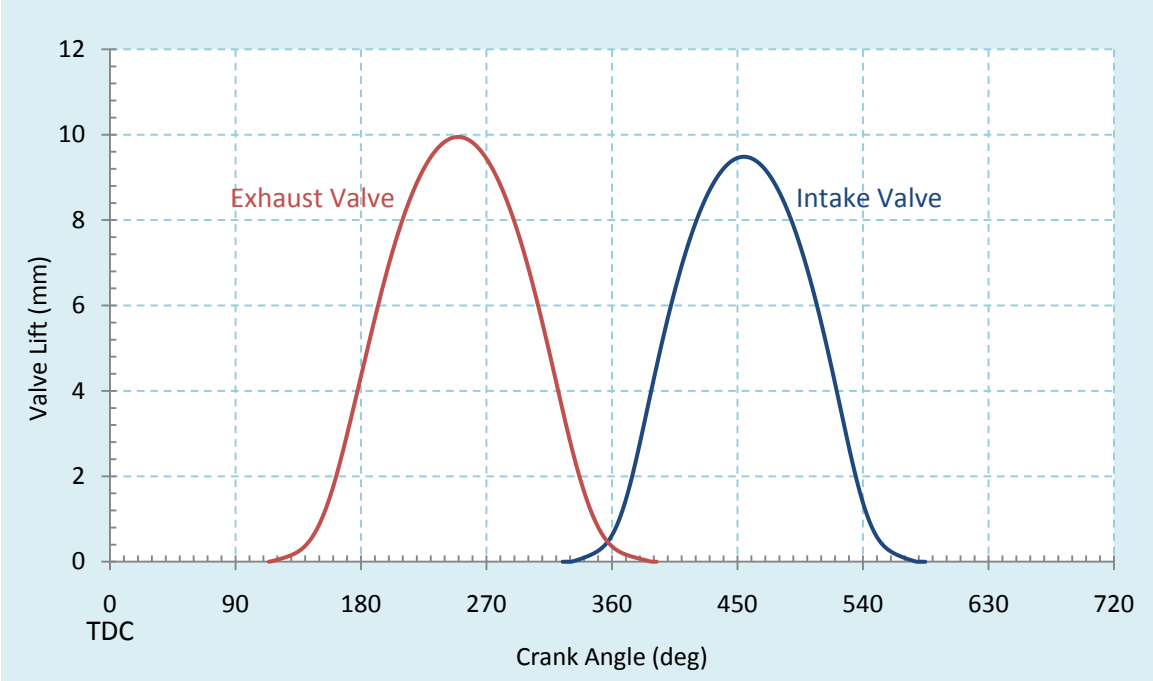

Fig.3 Intake and exhaust valve lift profile

The intake and exhaust ports into an engine's cylinder are modeled geometrically with pipes. According to the simulation, the flow coefficients of the valves include the flow losses caused by the port, so the friction and pressure loss for the intake and exhaust ports are set to zero in the model. For convenience, the wall temperature for the intake and exhaust ports are approximated to as 450 K and 550 K, respectively.

4.5 Modeling in-cylinder flow and heat transfer

4.5.1 In-cylinder flow model

The in-cylinder flow model breaks the cylinder into four regions: the squish region (I), head region (II), center region (III), and piston cup region (IV), as shown in figure 4 below.

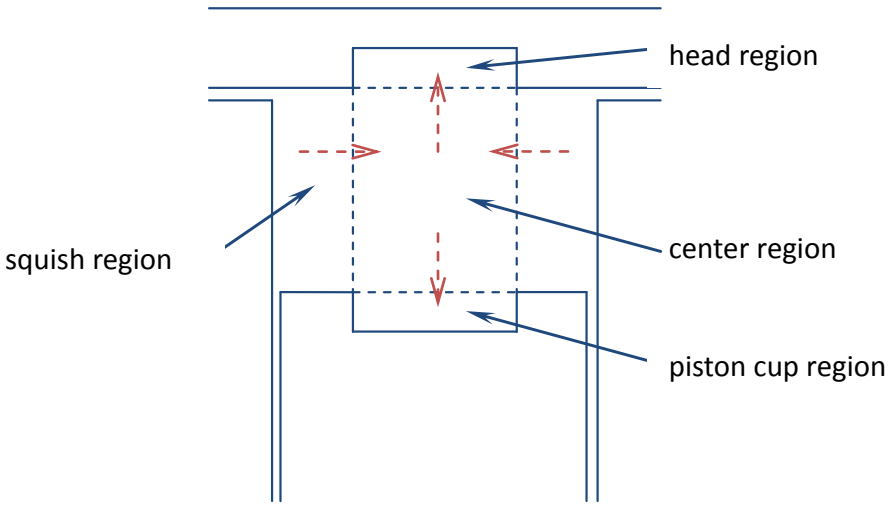

Fig.4 Flow regions appropriate for typical bowl-in-piston diesel engine geometries

At each time step in each region, the mean radial velocity, axial velocity, and swirl velocity are calculated taking into account the cylinder geometry, the piston motion, and flow rate/swirl/tumble of the incoming and exiting gases through valves. The flow model also includes single zone turbulence model which solves the turbulence kinetic energy equation and the turbulence dissipation rate equation. The resultant turbulence intensity and in-cylinder velocity are used in the combustion simulation and heat transfer calculation.

According to the data from engine manufacturer, swirl and tumble coefficients for the intake valves are specified versus L/D (lift over diameter), and these values are used to determine the swirl and tumble torque by the following equation. Swirl and tumble torque will be applied to the in-cylinder gases and therefore affect the in-cylinder flow solution.

$$Swirl\ Coefficient = \frac{2 \cdot T_s}{\dot{m}} \tag{4-10}$$

$$Tumble\ Coefficient = \frac{T_t}{\dot{m}} \tag{4-11}$$

$$U_{is} = \sqrt{RT_0}\left\{\frac{2\gamma}{\gamma - 1}\left[1 - P_r^{\frac{\gamma-1}{\gamma}}\right]\right\}^{1/2} \tag{4-12}$$

where: T_s = swirl torque

T_t = tumble torque

$\dot{m}$ = mass flow rate

U_{is} = isentropic valve velocity

D = cylinder bore

P_r = absolute pressure ratio

R = gas constant

T_0 = upstream stagnation temperature

γ = specific heat ratio

4.5.2 <u>In-cylinder heat transfer model</u>

(1) Woschni model

The in-cylinder heat transfer applied in the engine model is basically the Woschni model **[22]** which is described as follows.

$$Nu = \left(\frac{h_c B}{k}\right) = C\left(\frac{\rho \bar{v}_p B}{\mu}\right)^m = C\,\mathrm{Re}^m \tag{4-13}$$

where $\rho = \frac{p}{RT}$, $k \propto T^{0.75}$, $\mu \propto T^{0.62}$, $\bar{v}_p = w$, and $C = 0.035$

$$h_c = CB^{m-1} p^m w^m T^{0.75-1.62m} \tag{4-14}$$

where the local average gas velocity w is correlated as follows,

$$w = \left[C_1 \bar{v}_p + C_2 \frac{V_d T_r}{p_r V_r} (p - p_m) \right] \tag{4-15}$$

where V_d is the displaced volume;

p is the instantaneous cylinder pressure;

p_r, V_r, T_r are the pressure, volume and temperature at the reference state;

p_m is the motored cylinder pressure at the same crank angle as P.

For the gas exchange period: C_1=6.18, C_2=0

For the compression period: C_1=2.28, C_2=0

For the combustion and expansion period: C_1=2.28, C_2=3.24×10^{-3}

Woschni's correlation, with the exponent m equal to 0.8, can be summarized as:

$$h_c = C_{conv} 3.26 B^{-0.2} p^{0.8} w^{0.8} T^{-0.55} \tag{4-16}$$

where C_{conv} is the multiplier for convection heat transfer (def = 1.0)

(2) Hohenberg model

Based on the basic form of Woschni equation,

$$h_c = C_{conv} 3.26 B^{-0.2} p^{0.8} w^{0.8} T^{-0.55} \tag{4-17}$$

An attempt was made to give improved definitions of the individual terms used in the above equation for the heat transfer coefficient by Hohenberg in 1979 **[23]**.

The term, $\left[D^{-0.2} \right]$, makes allowance for the cylinder bore effect on the flow near the wall. However, since the cylinder volume V_C in IC engine changes periodically, Hohenberg applied the diameter $\overline{D}$ of a ball as a characteristic quantity where its volume corresponds to the momentary cylinder volume V_C:

$$V_C = \frac{\overline{D}^3 \cdot \pi}{6} \tag{4-18}$$

$$\overline{D} = C \cdot V_C^{0.33} \tag{4-19}$$

Hence,

$$D^{-0.2} = \overline{D}^{-0.2} = C \cdot V_C^{-0.066} \tag{4-20}$$

In order to compensate the variations in radiation which is known to increase with increasing diameters, the final form of this term become,

$$D^{-0.2} = C \cdot V_C^{-0.06} \tag{4-21}$$

The term, $\left[p^{0.8} T^{-0.53} \right]$, indicates that the heat transfer coefficient increases with rising $T^{-0.5}$ pressure and decreases with rising temperatures. After systematic tests with either varying pressure or varying temperature, it has been found out that the effect of temperature and pressure alone can be suitably defined by the following,

$$p^{0.6} \cdot T^{-0.5} \tag{4-22}$$

The term, $\left[v^{0.8} \right]$, describes the effect of flow velocity on heat transfer. However, the velocity is subjected to periodical changes so that the customary use of the mean piston speed only supplies information on the rise in the velocity level with increasing speed but not on the variations with crankshaft angle. The following points are relevant for the formulation of an equation to describe actual conditions: the intake swirl, turbulence caused by intake swirl, super-imposed flow, and turbulence caused by combustion. To approximate the above effect, the original term has been modified as follows,

$$v^{0.8} = p^{0.2} T^{0.1} \left(\bar{v}_p + C_2 \right)^{0.8} \tag{4-23}$$

The time-relation is described by $p^{0.2} T^{0.1}$, the mean piston speed $\bar{v}_p$ makes compensation for the rise in the velocity with increasing engine speed, and the constant C_2

for combustion turbulence and the relatively small radiation portion.

By summarizing the above equations, the heat transfer coefficient can be defined by the following expression (4-24):

$$h = C_1 \cdot V_C^{-0.06} \cdot p^{0.8} \cdot T^{-0.4} \cdot \left(\bar{v}_p + C_2\right)^{0.8} \qquad (4\text{-}24)$$

where

h	-	heat transfer coefficient	[W/m^2-K]
V_C	-	cylinder volume	[m^3]
p	-	in-cylinder pressure	[bar]
T	-	in-cylinder temperature	[K]
$\bar{v}_p$	-	mean piston speed	[m/s]
C_1, C_2	-	constants (typical values are C_1=130 and C_2=1.4)	

4.6 Modeling combustion and emission formation

The combustion model (DI-Jet Model) is a quasi-dimensional multi-zone combustion model for direct injection compression ignition engine. It is primarily used to predict burn rate and NOx emissions. Soot is also predicted, but the predicted concentrations are not particularly meaningful and should be used to study only trends in the results.

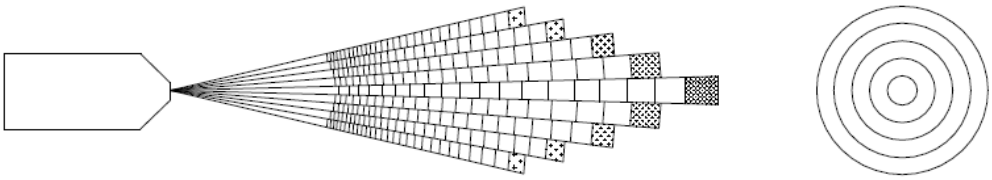

Fig.5 Injected mass is divided into many zones

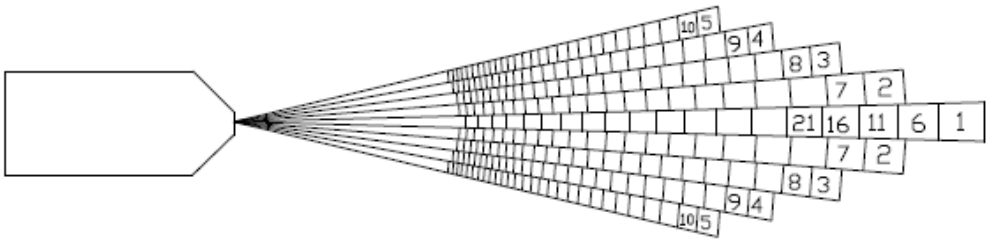

Fig.6 Numbering rule of the zones

As shown in figure 5, the total injected mass is divided into zones: 5 radial zones and a maximum of 80 axial zones (depending on the value specified in the 'EngCylCombDIJet' model) **[21]**. Figure 6 shows how the zones are numbered. At each timestep taken by the code during the injection period, an axial "slice" (five radial zones) is injected into the cylinder (if the time steps are very small, the fuel may be injected at only every other timestep). The total mass of fuel in all of the zones will be equal to the specified injection rate (mg/stroke) divided by the specified number of nozzle holes. (The DI-Jet model really models the plume from only one nozzle hole.) The mass of fuel in each axial "slice" is determined by the injection pressure at that timestep and the elapsed time since the last zones were injected. This mass injected at each timestep is divided equally between the five radial zones. The instantaneous injection pressure is also used to calculate the injection velocity of each axial slice.

Each zone additionally contains subzones for liquid fuel, unburned vapor fuel and entrained air, and burned gas. Immediately after a zone is injected, the zone is 100% liquid fuel. As the zone moves into the cylinder, it "entrains" air and the fuel begins to evaporate, thus forming the unburned subzone. The mass of the entrained air causes the velocity of the zone to decrease because momentum of the zone is conserved. The outer zones entrain air more quickly than the inner zones, thus decreasing their velocity more quickly and resulting in less penetration distance as can be seen in figure 5.

From the mass of vapor fuel and entrained air in each unburned subzone, the zonal fuel to air ratio is known. The zonal temperature is calculated taking into account the

temperature of the injected fuel, entrained air temperature, and the effects of the fuel evaporation. When the combination of cylinder pressure, zonal temperature, and fuel-to-air ratio becomes combustible, the fuel in the zone ignites, further changing the temperature and composition. All products of combustion will be moved to the burned subzone. NOx and soot are calculated independently in each burned subzone taking into account the fuel/air ratio and temperature. The total cylinder NOx and soot are the integrated total of all of the individual burned subzones.

4.6.1 Injection submodel

In the injection submodel, assume the flow through each nozzle is quasi-steady and one-dimensional, the instantaneous fuel flow rate through the nozzle, $\dot{m}_i$, is given by the following equation **[21]**:

$$\dot{m} \qquad \left(\frac{\rho_{fc}}{\rho_{fi}}\right)\sqrt{2\rho_{fi}\left(P_i - P_c\right)} \tag{4-25}$$

where C_n is the discharge coefficient;

A_n is the nozzle hole area;

ρ_{fi} is the density of the fuel in the injector;

ρ_{fc} is the density of the fuel in the cylinder;

P_i is the instantaneous injection pressure;

P_c is the instantaneous pressure in cylinder;

Since $\dot{m}_i = \rho_{fi} A_n U_i$ the fuel injection velocity at the nozzle tip U_i can be calculated as:

$$U_i = C_n\left(\frac{\rho_{fc}}{\rho_{fi}}\right)\sqrt{\frac{2\left(P_i - P_c\right)}{\rho_{fi}}} \tag{4-26}$$

Also, the total injected fuel per event can be related by the following equation **[21]**:

$$m_{total} = \int_{t_{inj\_start}}^{t_{inj\_end}} \dot{m} \tag{4-27}$$

In the program, the injected mass of fuel per event, m_{total} , and the injection pressure profile are needed to be specified in the "injector" object. From the pressure profile $\dot{m}_i$ can be calculated by equation (4-25) left C_n unknown. Then from equation (4-27) and the specified m_{total} , C_n can be calculated. The reasonable range for C_n is 0.6 to 0.8 and if the calculated C_n is out of this range, there might be something wrong with the pressure profile or specified m_{total} value.

4.6.2 Fuel spray dynamics

(1) Fuel jet penetration

The fuel enters the combustion chamber with a nominal centerline velocity equal to:

$$U_i = C_n \left(\frac{\rho_{fc}}{\rho_{fi}} \right) \sqrt{\frac{2\left(P_i - P_c\right)}{\rho_{fi}}} \tag{4-28}$$

where C_n is the discharge coefficient of the nozzle;

ρ_{fi} is the density of the fuel in the injector;

ρ_{fc} is the density of the fuel in the cylinder;

P_i is the instantaneous injection pressure;

P_c is the instantaneous pressure in cylinder;

The breakup time and the penetration distance at the centerline are given by **[21]**:

$$\begin{cases} S = U_i t \left[1 - 0.06 \left(\dfrac{t}{t_{br}} \right)^7 \right] & \text{for } t<t_{br} \\ S = U_i t_{br} \left[\left(t \cdot t_{br} \right)^{0.5} - 0.06 \right] & \text{for } t>t_{br} \end{cases} \tag{4-29}$$

$$t_{br} = C_{br} \times 0.29 \left(3 + L_n / D_n \right) \left(\frac{\rho_{fc}}{\rho_a} \right) \left(\frac{D_n}{U_i} \right) \tag{4-30}$$

where L_n/D_n is the aspect ratio of the nozzle;

C_{br} is the breakup time multiplier (def = 1.0)

Swirl (defined by swirl ratio R) affects the above axial penetration distance and modifies it by the following correlation **[21]**:

$$S_{swirl} = \frac{S}{1 + \frac{\pi RNS}{U_i}} \tag{4-31}$$

where R is the swirl ratio;

N is the engine speed;

S is the penetration distance without swirl effect;

The above set of equations describes the penetration of the centerline of the jet. The penetration of the jet away from the centerline is calculated from the same equation set except that the penetration equation is reduced by multiplying it with a radial velocity distribution function, which varies from 1.0 to 0.5, along the radial direction as follows **[21]**:

$$\begin{cases} S_r = e^{-ar} S = e^{-ar} U_i t \left[1 - 0.06 \left(\frac{t}{t_{br}} \right)^7 \right] & \text{for } t<t_{br} \\ S_r = e^{-ar} S = e^{-ar} U_i t_{br} \left[\left(t \cdot t_{br} \right)^{0.5} - 0.06 \right] & \text{for } t>t_{br} \end{cases} \tag{4-32}$$

The temperature of the injected fuel increases due to the frictional heating as it passes through the nozzle. This increase can be much significant in the modern high pressure injectors. The increase in fuel temperature due to friction during injection is given by the following correlation **[21]**:

$$\Delta T_f = \frac{P_i - P_c}{\rho_{fi} C} \left[1 - \left(\frac{P_i}{\rho_{fc}} \right) \left(\frac{\delta \rho}{\delta P} \right) - 1.02 C_n \left(\frac{\rho_{fi}}{\rho_{fc}} \right)^2 \right] \tag{4-33}$$

where $\frac{\delta \rho}{\delta P}$ is a term related to fuel compressibility;

C is the specific heat of the fuel.

(2) Breakup into droplets

The fuel breaks up into fine droplets, the diameter of which is calculated form a SMD correlation given as follows **[21]**:

$$\text{Nominal } SMD = 60 D_n \, \mathrm{Re}^{-0.22} \, \mathrm{We}^{-0.31} \left(\frac{\rho_{fc}}{\rho_a} \right)^{-0.17} \tag{4-34}$$

All the droplets in a zone are assumed to be identical in diameter. The SMD for the individual radial zones is calculated by multiplying the nominal SMD value by a profile which increases the centerline value to reflect the coagulation of droplets near the centerline due to higher droplet density, and decreases the SMD value for zones away from the centerline. The detailed correlation is given as follows **[21]**:

$$SMD_{centerline} = 60 C_{SMD,1} D_n \, \mathrm{Re}^{-0.22} \, \mathrm{We}^{-0.31} \left(\frac{\rho_{fc}}{\rho_a} \right)^{-0.17} \tag{4-35}$$

$$SMD_{2nd\ layer} = 60 C_{SMD,2} D_n \, \mathrm{Re}^{-0.22} \, \mathrm{We}^{-0.31} \left(\frac{\rho_{fc}}{\rho_a} \right)^{-0.17} \tag{4-36}$$

$$SMD_{3rd\ layer} = 60 C_{SMD,3} D_n \, \mathrm{Re}^{-0.22} \, \mathrm{We}^{-0.31} \left(\frac{\rho_{fc}}{\rho_a} \right)^{-0.17} \tag{4-37}$$

$$SMD_{4th\ layer} = 60 C_{SMD,4} D_n \, \mathrm{Re}^{-0.22} \, \mathrm{We}^{-0.31} \left(\frac{\rho_{fc}}{\rho_a} \right)^{-0.17} \tag{4-38}$$

$$SMD_{5th\ layer} = 60 C_{SMD,5} D_n \, \mathrm{Re}^{-0.22} \, \mathrm{We}^{-0.31} \left(\frac{\rho_{fc}}{\rho_a} \right)^{-0.17} \tag{4-39}$$

where $C_{SMD,1}$ is the SMD profile multiplier for the axial zones (def = 1.35)

$C_{SMD,2}$ is the SMD profile multiplier for the 2nd radial zones (def = 1.19)

$C_{SMD,3}$ is the SMD profile multiplier for the 3rd radial zones (def = 1.01)

$C_{SMD,4}$ is the SMD profile multiplier for the 4th radial zones (def = 0.85)

$C_{SMD,5}$ is the SMD profile multiplier for the 5th radial zones (def = 0.74)

(3) Air entrainment

As the jet develops, it entrains air and residuals from the initial charge of the cylinder. The entrainment is nominally calculated from the conservation of the initial jet momentum. The initial momentum of zone is calculated from the injection velocity (U_i) and fuel mass (m_f). The fuel zone decelerates according to the prescribed expression given above. Using the principle of conservation of momentum, the total amount of air it entrained (m_a) at any instant can be calculated and conveniently expressed as a multiple of the fuel mass in that zone **[21]**:

$$m_a = m_f \left[\frac{U_i}{dS/dt} - 1 \right] \tag{4-40}$$

The rate of air entrainment in any given time step can be calculated s a derivative of the above expression. Before and after ignition, the rate of entrainment is respectively set to:

$$\text{before ignition:} \quad dm_{a1}/dt = C_b \, dm_a/dt \tag{4-41}$$

$$\text{after ignition:} \quad dm_{a1}/dt = C_a \, dm_a/dt \tag{4-42}$$

where C_b is the entrainment multiplier before combustion (def = 1.2)

C_a is the entrainment multiplier after combustion (def = 0.5)

After jet impingement on the bowl surface, a wall jet is formed along the bowl sidewall. The entrainment rate is further modified to account for the development of the wall jet along the bowl surface:

$$dm_{a2}/dt = C_w \, dm_{a1}/dt \tag{4-43}$$

where C_w is the entrainment multiplier after wall impingement (def = 1.2)

(4) Evaporation of the droplets

Once the droplets have been injected, they begin to evaporate and their diameters reduces gradually. The evaporation rate is strongly dependent on the relative velocity of the droplet. It is assumed that the drag acting on the droplets reduces their speed rapidly according to the following differential equation based on the Stokes drag law:

$$\frac{\delta U_d}{\delta t} = -\frac{18 U_d \mu}{\rho D_d^2} - \frac{3 U_d}{D_d} \cdot \frac{\delta D_d}{\delta t} \tag{4-44}$$

The solution of the above equation yields an exponential decay function, with a time constant proportional to D_d^2/υ. Once the droplets have slowed down to the velocity of the surrounding gas, the Sherwood number for evaporation rate and the Nusselt number for convective heat transfer go to 2. The evaporation of the droplet can be diffusion-limited or boiling-limited. In the diffusion-limited case, the evaporation rate per droplet is given by **[21]**:

$$\frac{dm_v}{dt} = G \pi D_d^2 \tag{4-45}$$

where $G = \rho \cdot Sh \cdot \alpha \ln \frac{1+\beta}{D_d}$

$$\beta = \frac{Y_o - Y_\infty}{1 - Y_\infty}$$

$$\mathrm{Sh} = 2 + 0.57 \mathrm{Sc}^{1/3}\, \mathrm{Re}^{1/2}$$

$$\mathrm{Re} = \frac{\rho U D_d}{\mu}$$

$$\mathrm{Sc} = \frac{\mu}{\rho \alpha}$$

α is the mass diffusivity

D_d is the diameter of a droplet

4.6.3 Ignition and combustion model

(1) Ignition delay submodel

The ignition delay is calculated for each unburned subzone separately. The calculation is based on the concept of an ignition integral (I), integrating a kinetic expression for the rate of ignition as described below **[21]**:

$$\begin{cases} \tau = \dfrac{Ai \times 10 - 6}{\phi\left(3-\phi\right)^{2}} P^{Bi} \exp\left(\dfrac{C_i}{T}\right) & \text{for } \phi < 3.0 \\ \tau = \infty \text{ for } \phi > 3.0 \end{cases} \tag{4-46}$$

where,

Ai : Overall Multiplier for ignition delay (def = 1.0)

Bi : Multiplier to the exponent for pressure dependence (def = -1.25)

Ci : Activation Temperature (def = 4000)

$$I = \int_{t_{inj}}^{t_{ign}} \frac{dt}{\tau} \tag{4-47}$$

Ignition is considered to have occurred when the value of the integral I becomes equal to one. Note that the dependence on the equivalence ratio has a minimum around 1.5 and approaches infinity at the lean and rich limits of 0 and 3, respectively.

(2) Combustion submodel (combustion kinetic rate correlation)

The combustion model is formulated so that it can handle both mixing and kinetics limited combustion, and a smooth transition from one to the other. Under normal conditions the combustion in a diesel engine is mixing limited, i.e. that it proceeds at a rate limited only by the availability of fuel vapor and oxygen at the right proportion. In these case, the rate at which the combustion kinetics proceeds is considered to be so rapid that it provides no additional limit on the combustion process. However, when the gas temperature is low, the combustion kinetics slows down exponentially, and at some point becomes the limiting factor. This can occur at cold start, and also at the latter parts of the expansion process. The kinetics can also slow down when the mixture is very lean.

For each zone, the kinetic rate of combustion in term of fuel consumption is determined by equation (4-48) **[21]**:

$$\begin{cases} \dfrac{dm_k}{dt} = A_c \phi \left(3.0 - \phi\right)^2 P^{B_c} \exp\left(-\dfrac{C_c}{T}\right) & \text{for } \phi < \\ \dfrac{dm_k}{dt} = 0 & \text{for } \phi > 3.0 \end{cases} \qquad (4\text{-}48)$$

where m_k is the burned mass of fuel in a specific zone

A_c is the overall combustion rate multiplier (def = 1.0)

B_c is the multiplier to the exponent for pressure dependence

C_c is the activation temperature for combustion kinetics

If the combustion is kinetically limited, the fuel is consumed at the rate dictated by the above equation. In such a case, the mass of fuel calculated by equation (D-3) plus mass of air proportional to the air/fuel ratio of the unburned subzone are transferred from a unburned subzone to the corresponding burned subzone. If the combustion is mixing controlled, i.e. the amount fuel available in the unburned subzone is less than the one prescribed by equation (D-3), only the available fuel is burned. In both cases, however, care is taken such that the burned subzone equivalence ratio never exceeds the carbon limit. It should be noted that once the unburned zone is fully consumed, fuel energy may continue to be released due to oxidation of burned subzone species as the burned subzone is further diluted by the entrained air.

4.6.4 Submodels for emission formation

(1) Submodel for NOx prediction

As mentioned above, NOx is calculated independently in each burned subzone and the total NOx emission is the summation of the NOx of each individual burned subzone. In each burned subzone, NOx calculation is primarily based on the extended Zeldovich mechanism. k1, k2, and k3 are the rate constants (from **[24]**) that are used to calculation the

reaction rates of the three equations below, respectively.

$$N_2 \text{ oxidation rate equation:} \qquad O + N_2 \longleftarrow \qquad + N \tag{4-49}$$

$$N \text{ oxidation rate equation:} \qquad N + O_2 \longleftarrow \qquad + O \tag{4-50}$$

$$OH \text{ reduction rate equation:} \qquad N + OH \longleftarrow \qquad + H \tag{4-51}$$

$$k_1 = 7.60 \times 10^{10} \times e^{\frac{-38000 \times C_{act}}{T_b}} \tag{4-52}$$

$$k_2 = 6.40 \times 10^{6} \times T_b \times e^{\frac{-3150}{T_b}} \tag{4-53}$$

$$k_3 = 4.10 \times 10^{10} \tag{4-54}$$

where T_b is the temperature for burned subzone, and C_{act} is the multiplier for activation temperature.

(2) Submodel for soot prediction

The submodel for soot prediction is based on two-step empirical soot model which was established by Hiroyasu et al. in 1985 **[25]**. It considers the soot formation process as involving two reaction steps: one is the formation step, in which soot is linked directly to molecular fuel vapor; and the other is the oxidation step, which describes the destruction of soot particles by molecular oxygen. Details are shown in table 2 (see next page).

Table 2 Soot kinetics and the corresponding rate constants

Step	Chemical Reaction	Reaction Rate
1	$Fuel \xrightarrow{\quad} C_{soot}$	$M_{fuel} p^{0.5} \exp\left(-\frac{8\times10^4}{RT}\right)$
2	$A_{site} + O_2 \xrightarrow{k_A} SurfaceOxide$ $SurfaceOxide \xrightarrow{k_A/k_Z} 2CO + A_{site}$ $B_{site} + O_2 \xrightarrow{k_B} 2CO + A_{site}$ $A_{site} \xrightarrow{k_T} B_{site}$	$\left(\frac{k_A p_{O2}}{1+k_Z P_{O2}}\right) x_A + k_B p_{O2}(1-x_A)$ $x_A = (1+k_T/k_B p_{O2})^{-1}$ $k_A = 20\exp(-15100/T)$ $k_B = 4.46\times10^{-3}\exp(-7640/T)$ $k_T = 1.51\times10^{5}\exp(-48800/T)$ $k_Z = 21.3\exp(2060/T)$

4.7 Modeling turbocharging system

4.7.1 Modeling the compressor and turbocharger

Turbine and compressor performance are modeled in GT-Power using performance maps that are provided by the user. Both compressor and turbine maps can be summarized as a series of performance data points, each which describes the operating condition by speed, pressure ratio, mass flow rate, and thermodynamic efficiency. The maps are configured so that if the speed and pressure ratio (or mass flow rate) is known, efficiency and mass flow rate (or pressure ratio) can be looked up in the maps. The compressor and turbine maps applied in this project are shown in figure 7 and 8.

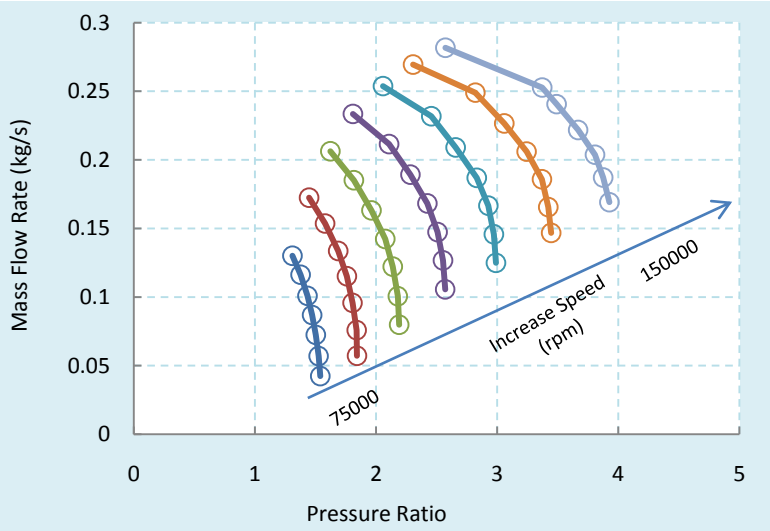

Fig.7 Compressor maps

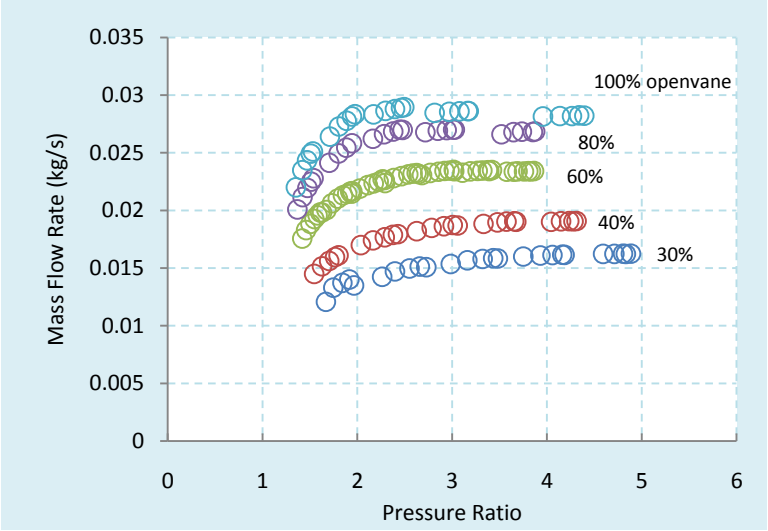

Fig.8 Turbine maps

At each timestep, speed and pressure ratio for both compressor and turbine are predicted by the code, and then the mass flow rate and efficiency are looked up in the table and imposed in the solution.

The imposed outlet temperature is calculated using the change in enthalpy across the turbine and compressor. The enthalpy change, and consequently, the power produced/consumed by turbine/compressor is calculated from the efficiency. The equations are shown as follows **[21]**:

Compressor:

$$h_{out} - h_{in} = \frac{\Delta h_s}{\eta_s} \tag{4-55}$$

$$\Delta h_s = c_p T_{tot,in} \left(PR^{\frac{\gamma-1}{\gamma}} - 1 \right) \tag{4-56}$$

$$P = r^{\cdot} \quad) \tag{4-57}$$

Turbine:

$$h_{out} - h_{in} = \eta_s \Delta h_s \tag{4-58}$$

$$\Delta h_s = c_p T_{tot,in} \left(1 - PR^{\frac{\gamma-1}{\gamma}} \right) \tag{4-59}$$

$$P = r^{\cdot} \quad) \tag{4-60}$$

where the total temperature is defined as $T_{tot,in} = T_{in} + \frac{u_{in}^2}{2c_p}$.

4.7.2 Modeling the intercooler

The air-to-air intercooler model applied here is a so-called semi-predictive model. The model does not solve the flow equation and energy equation in the intercooler. Instead, based on the inlet temperature, ambient temperature, and the empirical effectiveness of the intercooler, the outlet temperature of the intercooler could be calculated by the following expression:

$$T_{out} = T_{in} - \eta_{ic} \times (T_{in} - T_{ambient}) \tag{4-61}$$

Since this is an air-to-air intercooler for the charged air, the effectiveness is a function of vehicle speed and the flow rate through the intercooler. The effectiveness table are shown in table 3.

Table 3 Effectiveness of the intercooler

Flow Rate (kg/s) / Vehicle speed (mile/hr)	0.01	0.05	0.1	0.15	0.2
0	0.6	0.58	0.56	0.54	0.35
10	0.65	0.63	0.61	0.58	0.55
20	0.66	0.64	0.63	0.62	0.6
40	0.7	0.67	0.65	0.64	0.61
60	0.7	0.69	0.67	0.66	0.63
80	0.71	0.7	0.69	0.68	0.66
100	0.71	0.7	0.7	0.69	0.68

5. RESULTS AND DISCUSSION

5.1 Engine specification

A 4.5 liter, inline 4 cylinder John Deere engine was selected for the present study. Engine specifications are listed in Table 4.

Table 4 Engine specification

Item	Unit	Value
Engine Type		4-stroke
No. of Cylinders		4 inline
Firing Order		1-3-4-2
Displacement	Liter	4.5
Compression Ratio		16.6
Bore	mm	106
Stroke	mm	127
Connecting Rod Length	mm	200
Wrist Pin to Crank Offset	mm	0
TDC Clearance Height	mm	1.3
Valve Configuration		4 valves/cylinder, OHV, Roller Lifter
Injection System		Common rail system
EGR System		Intercooled, high pressure EGR
Turbocharging System		Variable geometry turbine, compressor with air-to-air intercooler

5.2 Validation methodology

The model was first validated by the experimental data at a motored condition. Then, by comparing computed pressure diagram and heat release curves with experimental results, the model was calibrated and validated at 9 firing operating conditions as shown in figure 9. In addition, it should be noted that, since the rack position map for the variable geometry turbine equipped with the engine is still not available, all simulations in the thesis were conducted using compressor-out (the pressure and temperature measured out of compressor) and turbine-in (pressure and temperature measured before turbine) conditions.

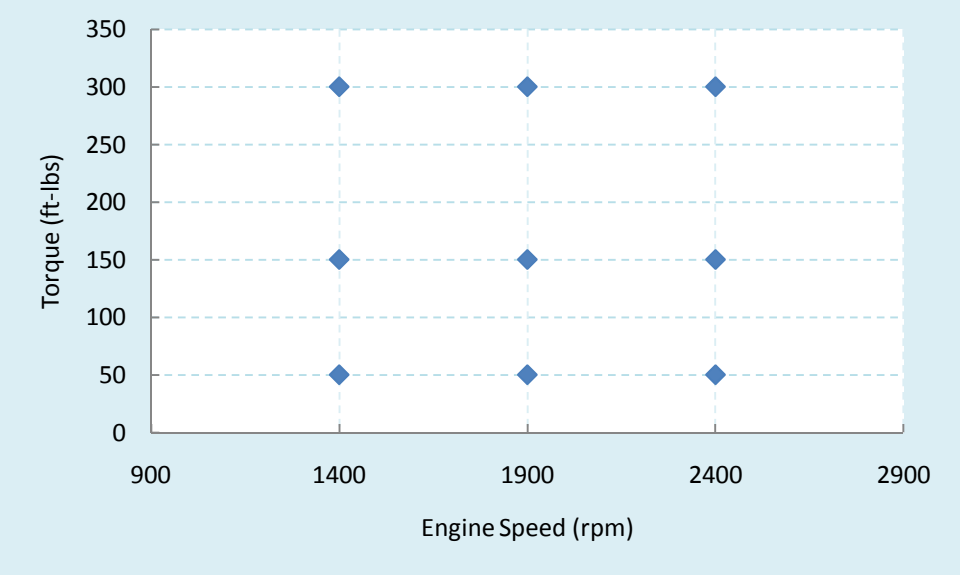

Fig.9 The 9 operating points matrix

5.3 Model calibration and validation

5.3.1 Validation at motored condition

To validate the model with experimental data, the first step is to compare the results at a motored condition. For a motored condition, no fuel is injected into the cylinder and no combustion will be initiated. The cylinder pressure for motored condition would only reflects the simple compression, expansion, and gas exchange process.

Figure 10 shows the cylinder pressures from the measurements and simulation. The good agreement between the two indicates that the cylinder geometry and heat transfer are accurately modeled in the simulation. Since the intake manifold pressure and temperature also have good agreement, the pressure drop between air inlet and intake manifold is also accurately modeled.

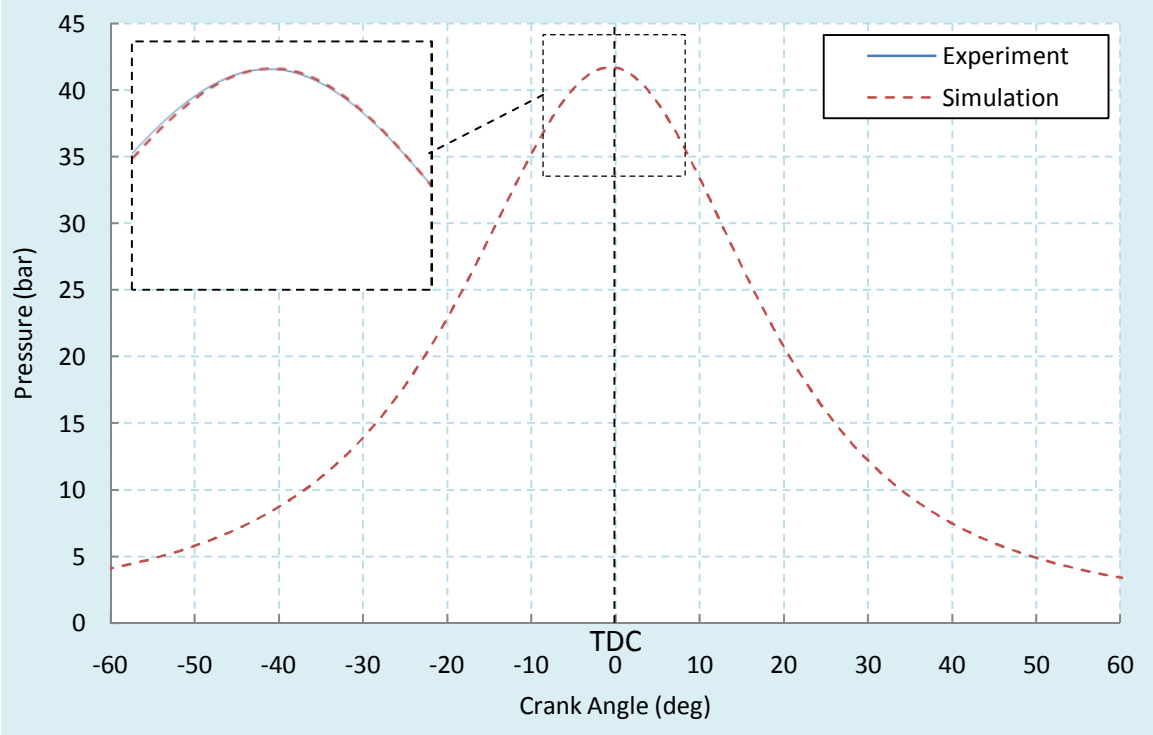

Fig.10 Model validation at the motored condition @ 1400 rpm

5.3.2 Model validation for firing cases

Based on the trial and error method, model was validated by matching the predicted pressure diagram and heat release rate with experimental results at each operating condition described earlier. Combustion rate multiplier and breakup length multiplier are adjusted to match the simulations with the experiments, and therefore these two parameters change with operating conditions; and all other model constants remain the same with respect to operating conditions.

First, engine performance (torque) of 9 points are compared in the following two figures. Figure 11 shows good agreement between predicted torque and the measured ones from experiment. Figure 12 shows the percent difference between the simulation and the experiment, and it has shown that the biggest difference (about 20%) occurs at 1900 rpm and 150 ft-lbs. At the low and medium load conditions, the simulation over-predicted the torque a little bit, while at the high load conditions, the simulation under-predicted the torque by about 10% in average. In general, the performance of the engine is predicted well enough.

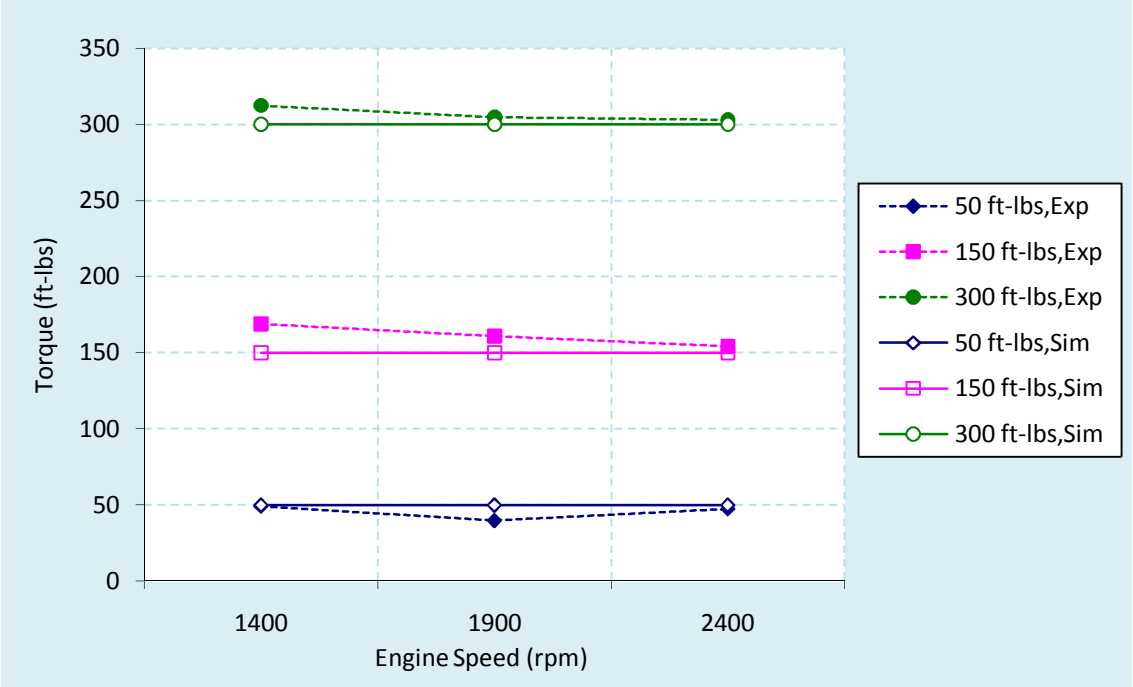

Fig.11 Engine performance comparison of simulation and measurement

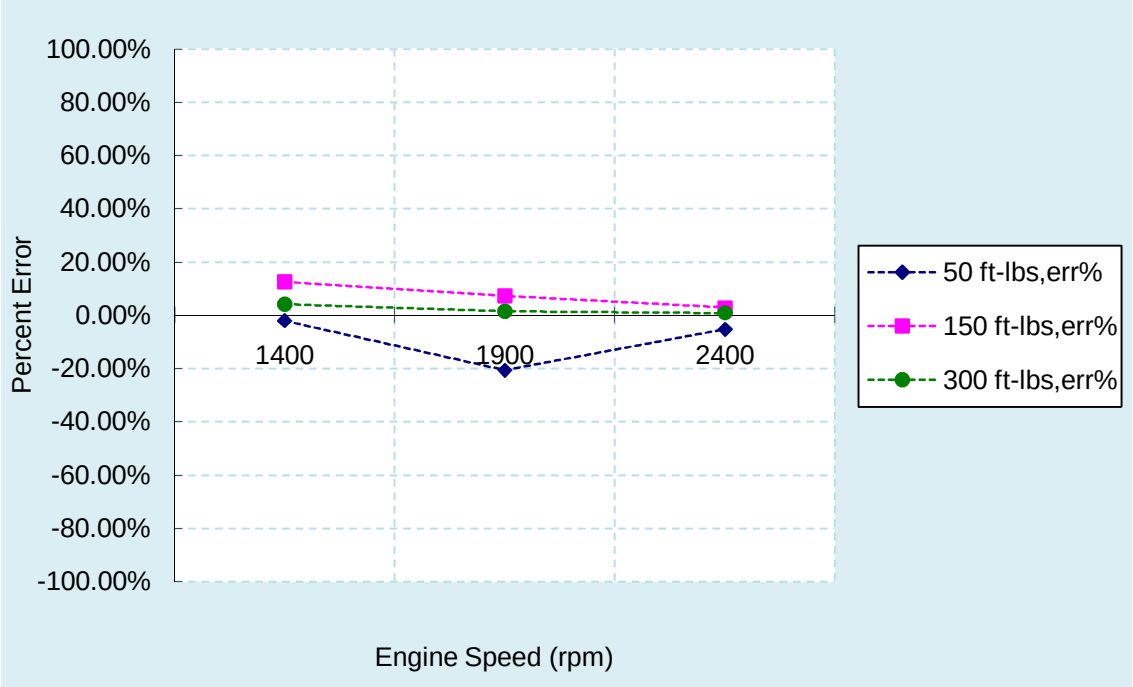

Fig.12 Difference of engine performance between simulation and measurement

The following figures compare pressure and heat release at each operating condition, which reveals more in-cylinder information and is very important in validating the model. Figures 13 and 14 show the pressure and heat release comparison at 1400 rpm 50 ft-lbs. These results show that the computed pressure match the measurement, while the predicted heat release misses the first peak (due to the pilot injection) and matches the main one.

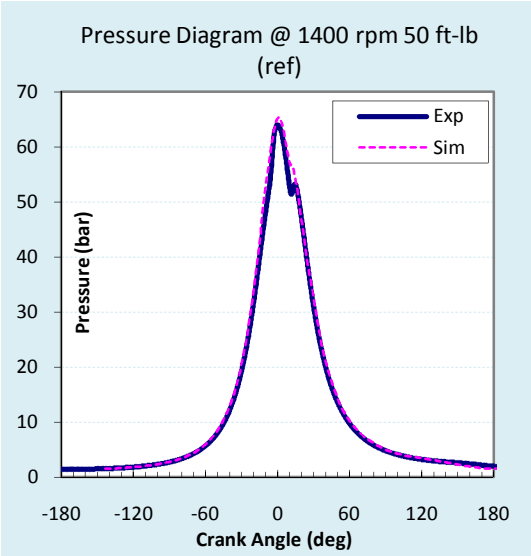

Fig.13 Pressure diagram comparison @ 1400 rpm 50 ft-lbs

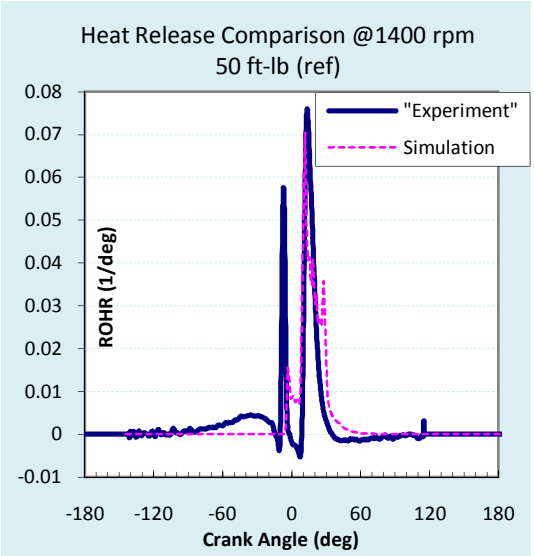

Fig.14 Heat release curve comparison @ 1400 rpm 50 ft-lbs

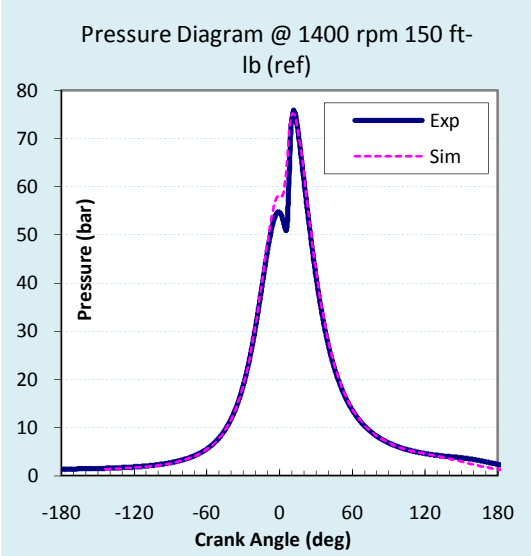

Fig.15 Pressure diagram comparison @ 1400 rpm 150 ft-lbs

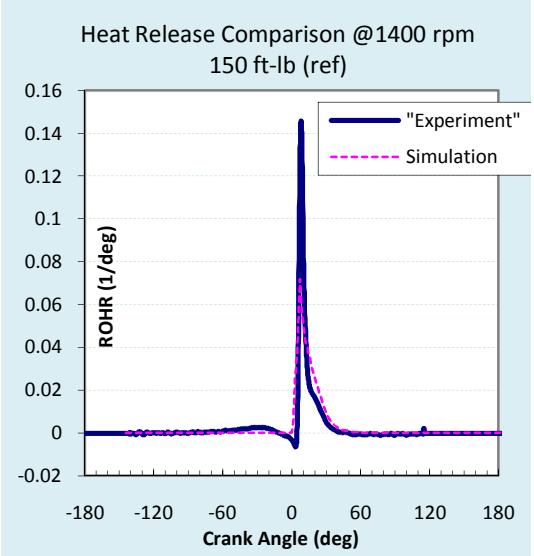

Fig.16 Heat release curve comparison @ 1400 rpm 150 ft-lbs

Figures 15 and 16 compare pressure and heat release at 1400 rpm and 150 ft-lbs. Similar to the previous condition, the pressure diagram matches except for an over-predicted first peak. For the heat release, the experiment has very high peak while the simulation has a lower peak but a longer heat release period. This discrepancy might

come from an approximated injection pressure which is taken as input for the simulation. Generally, high injection pressure would lead to high heat release peak.

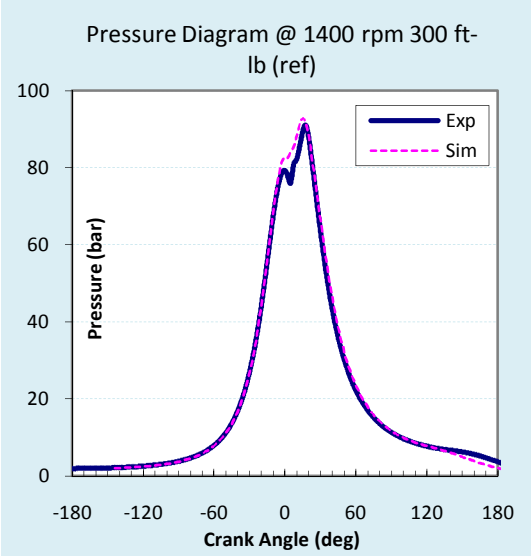

Fig.17 Pressure diagram comparison @ 1400 rpm 300 ft-lbs

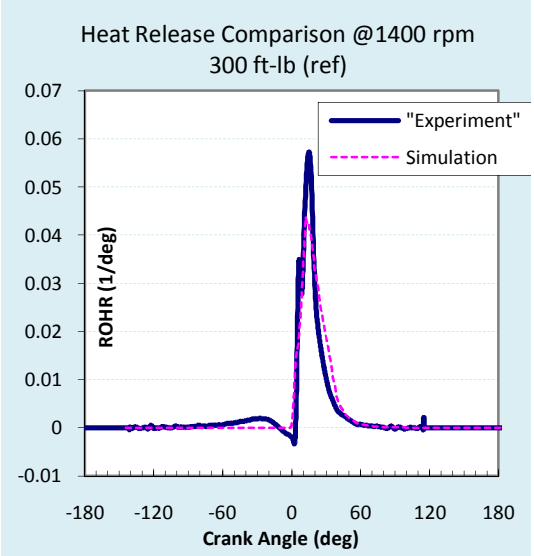

Fig.18 Heat release curve comparison @ 1400 rpm 300 ft-lbs

Figures 17 and 18 compares pressure and heat release at 1400 rpm and 300 ft-lbs. This case is very similar to the 1400 rpm and 150 ft-lbs case. The simulation predicted the pressure pretty well, but somewhat under-predicted the heat release peak by about 25%. However, in general, for the three cases at low engine speed (1400 rpm), the model accurately predicted several important parameters and is validated by the measurement from experiments.

The following 6 figures (see figures 19, 20, 21, 22, 23, and 24) show the model validation at 1900 rpm with 50 ft-lbs, 150 ft-lbs, and 300 ft-lbs load. For all the three cases, the code over-predicts the peak of the in-cylinder pressure by 5%-10%, while the compression and expansion processes match the measurements well. Many engine operating factors could affect the pressure trace prediction, such as compression ratio, injection timing, injection profile. Also many calibration factors affect the pressure diagram significantly, such as combustion rate multiplier, breakup length multiplier, and

wall temperature. For this work, the compression ratio and injection timing have been determined by measurement, but the injection profile was not known. The approximated injection pressure might not reflect the real case correctly which leads to different heat release rate, combustion rate, and finally pressure trace. But in general, the difference between prediction and measurement is still in an acceptable range, considering the existence of the uncertainty of the experiments.

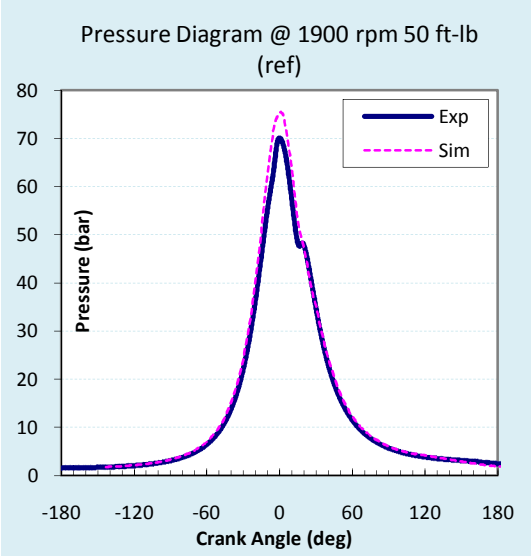

Fig.19 Pressure diagram comparison @ 1900 rpm 50 ft-lbs

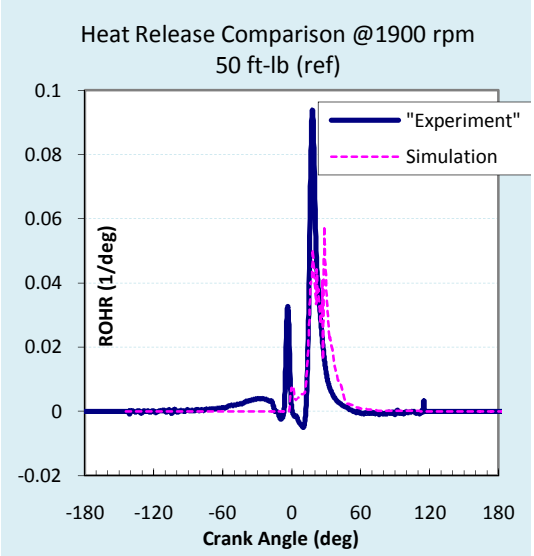

Fig.20 Heat release curve comparison @ 1900 rpm 50 ft-lbs

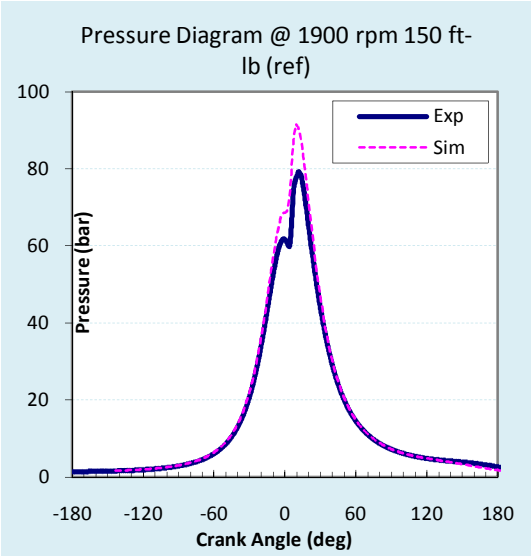

Fig.21 Pressure diagram comparison @ 1900 rpm 150 ft-lbs

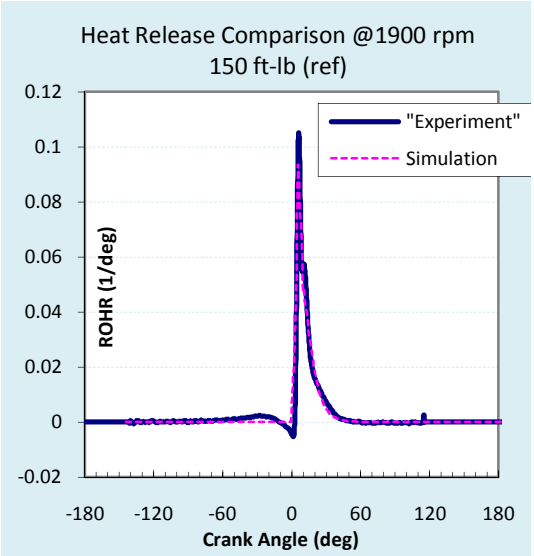

Fig.22 Heat release curve comparison @ 1900 rpm 150 ft-lbs

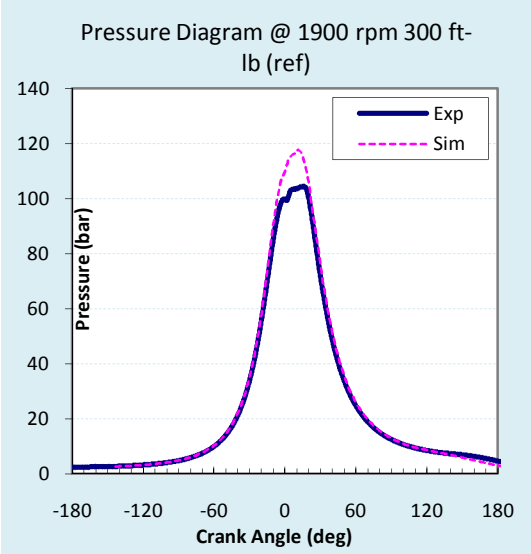

Fig.23 Pressure diagram comparison @ 1900 rpm 300 ft-lbs

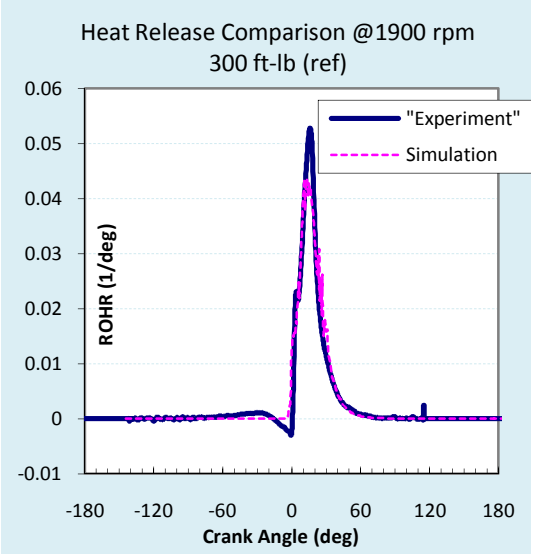

Fig.24 Heat release curve comparison @ 1900 rpm 300 ft-lbs

In the above three cases, the simulation predicts the single injection cases better than the multiple injection cases. For the 1900 rpm 50 ft-lbs case and the earlier 1400 rpm 50 ft-lbs case, both of the predicted heat release curves miss the first peak which was a results of pilot injection.

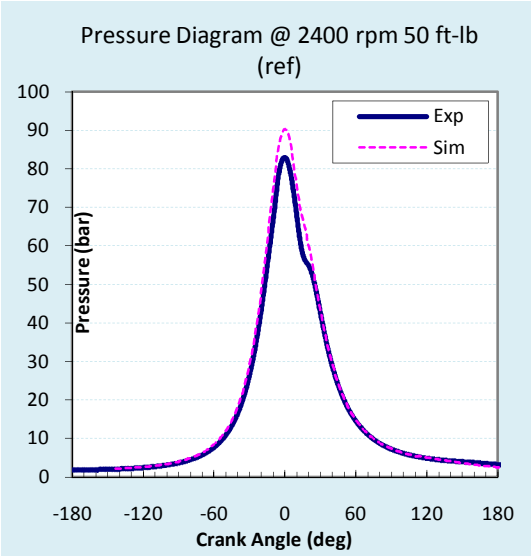

Fig.25 Pressure diagram comparison @ 2400 rpm 50 ft-lbs

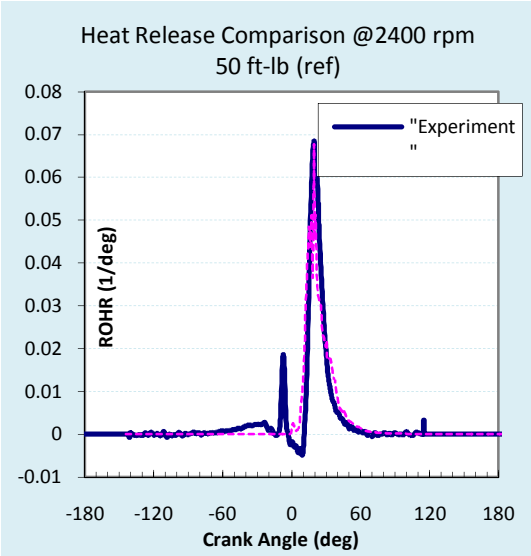

Fig.26 Heat release curve comparison @ 2400 rpm 50 ft-lbs

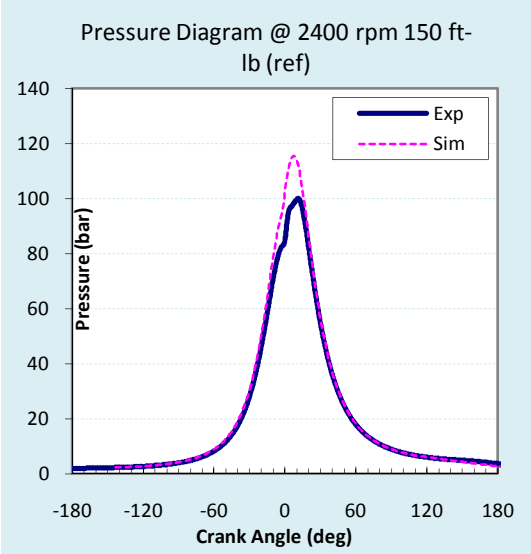

Fig.27 Pressure diagram comparison @ 2400 rpm 150 ft-lbs

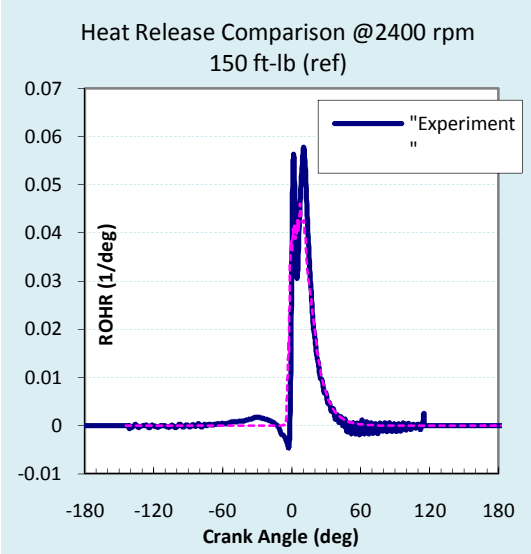

Fig.28 Heat release curve comparison @ 2400 rpm 150 ft-lbs

The validation of the last three operating conditions at 2400 rpm are shown from figures 25, 26, 27, 28, 29, and 30. Very similar to the cases at 1900 rpm, peak pressure is somewhat over-predicted comparing to the measurement from experiment. Combustion rate and injection pressure profile are still the two major reason for the discrepancy.

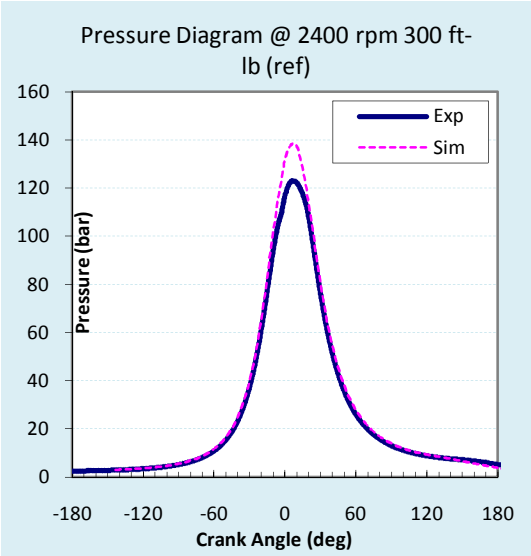

Fig.29 Pressure diagram comparison @ 2400 rpm 300 ft-lbs

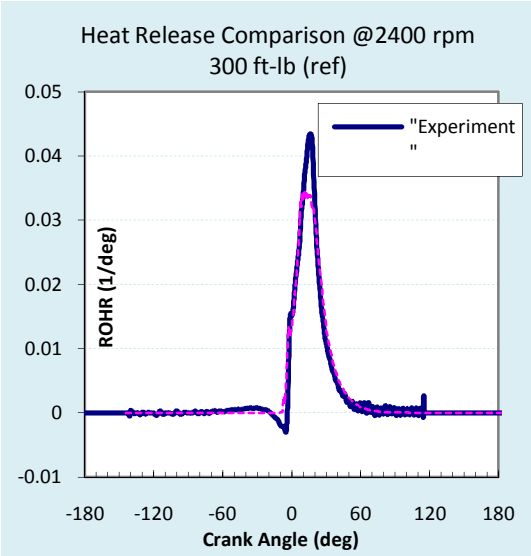

Fig.30 Heat release curve comparison @ 2400 rpm 300 ft-lbs

In this section, model is validated at the all 9 operating conditions. All of this work are based on diesel fueled engine results, since diesel fuel is better studied and has more accurate fuel properties available. For completeness, the simulations have also been used for the biodiesel cases. The detailed biodiesel validations are shown in Appendix III.

5.4 Results for parametric study

Parametric studies are most useful if the engine speed and load are held constant at some selected values which are representative of the typical operating modes. For the present study, an engine speed of 1900 rpm and a load of 150 ft-lbs were chosen as the reference point for the following parametric studies. Additional computations were completed at 1400 rpm and 2400 rpm, and the load of these speeds range from 50 ft-lbs to 300 ft-lbs.

Besides the load/speed variation, the engine variables selected for the parametric analysis were: injection timing, injection pressure, EGR percentage, and compression ratio. Table 5 lists the structure of the parametric study. In each part of the study all

variables were held constant at the value of base case except for the one which is being studied.

Table 5 Structure of the parametric studies

	Engine Speed (rpm)	Torque (ft-lbs)	Injection Timing (deg aTDC)	Injection Pressure (bar)	EGR (%)	r_c
Base Case	1900	150	-5 (-6.4*)	1000	0	16.6
Injection Timing	1900	150	-15 ~ +5	1000	0	16.6
Injection Pressure	1900	150	-5	600~1400	0	16.6
Load/Speed	1400~2400	50 ~ 300	varies	varies	varies	16.6
EGR level	1900	150	-5	1000	0~40	16.6
Compression Ratio	1900	150	-5	1000	0	14.6~18.6

* For biodiesel case, the injection timing for the base condition is 6.4 deg bTDC.

5.4.1 Injection timing variation

The effect of variations in injection timing on the pressure trace for the diesel case is shown in figure 31. The injection timings are varied from 10 deg advanced to 10 deg retarded to base case, and there are five timings being studied in total.

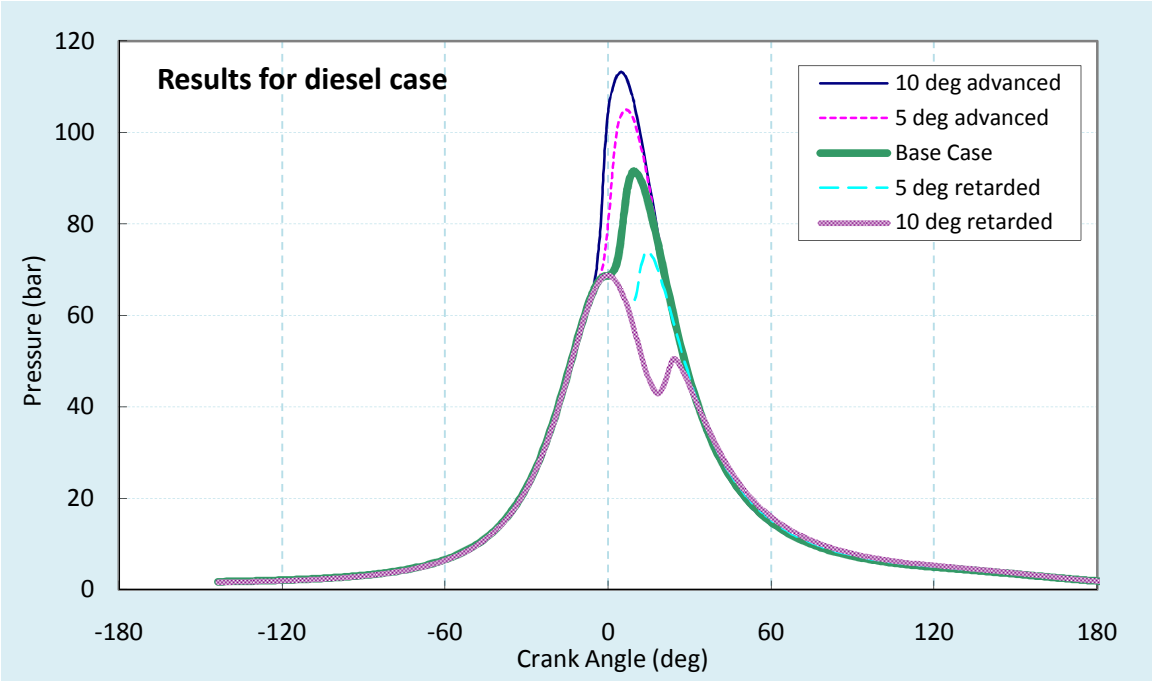

Fig.31 Pressure diagram for different injection timing, diesel case

Advanced injection timing leads to higher in-cylinder pressure while retarded injection timing lowers the pressure. This effect can be attributed to the start of combustion in the cylinder. If fuel is injected into the cylinder early, the combustion starts during the compression stroke, and thereafter gas pressure and temperature increase rapidly due to combustion. In the mean time, the piston continues going up which cause the gas pressure and temperature to increase more rapidly. These two effects combine together and then create a high peak in gas pressure. On the other hand, if the combustion start is after TDC (top dead center), the pressure decreases due to expansion offset the pressure rises due to combustion, which leads to a relatively lower gas pressure. If the injection is retarded too much, as can be seen in the “10 deg retarded” case, the pressure trace in-cylinder would show two peaks rather than one peak as for the other cases. The first peak is mostly due to the compression stroke and the second peak is due to the heat release (combustion).

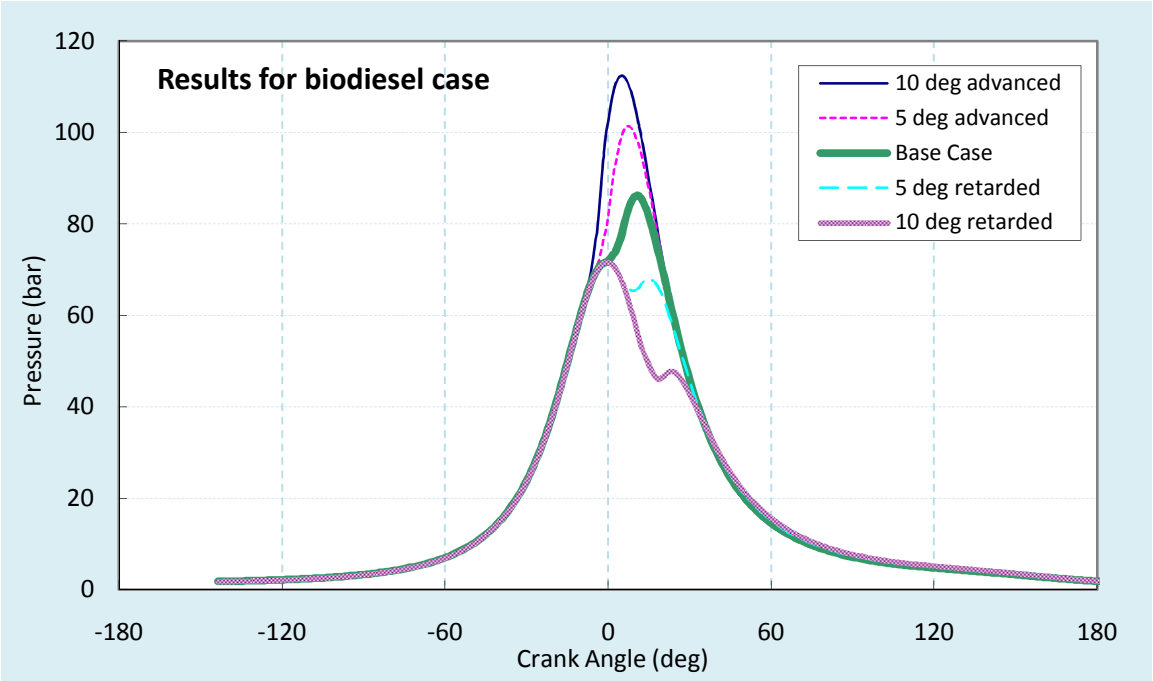

Fig.32 Pressure diagram for different injection timing, biodiesel case

For biodiesel case, figure 32 shows the effect of injection timing variation on the pressure diagram. The effect of injection timing for the biodiesel case is very similar to that of diesel case, except that the absolute values may not be the same. The 10 deg advanced injection timing approximately increases the peak of gas pressure by 30%, while the 10 deg retarded injection timing lowers the peak pressure by about 20% (and creates an additional peak). As documented earlier, the timing of combustion start is the major factor affecting the pressure diagram.

The effect of injection timing on ignition delay is showed in figure 33 and results for diesel and biodiesel case are compared. From the plot, ignition delay increases when retarding the injection timing from the base timing, and ignition delay also increases when advancing the injection timing from the base case. This is a very typical plot in engine operation and there is a “best” timing (at which the engine has the shortest ignition delay). Too advanced injection timing leads to longer mixing time due to low temperature and low pressure in the cylinder, and therefore leads to longer ignition delay.

For the similar reason, when injection timing is retarded to very late, ignition delay will also increase due to decreasing pressure and temperature in the cylinder. Comparing the biodiesel results with the diesel results, shows that the trends of ignition delay change are pretty similar to each other, while the biodiesel fueled cases have relatively longer ignition delay than those of diesel fueled cases.

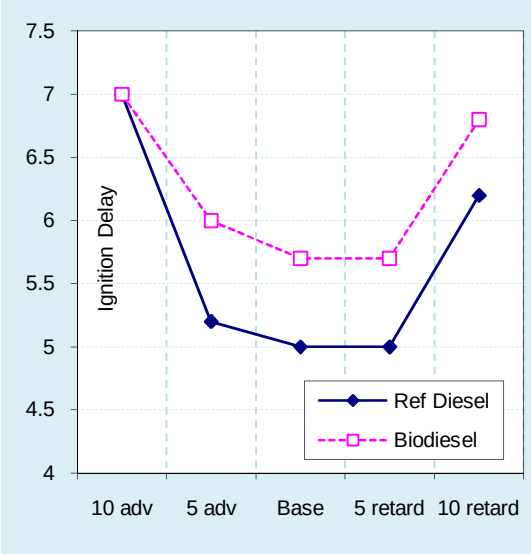

Fig.33 Ignition delay for different injection timings

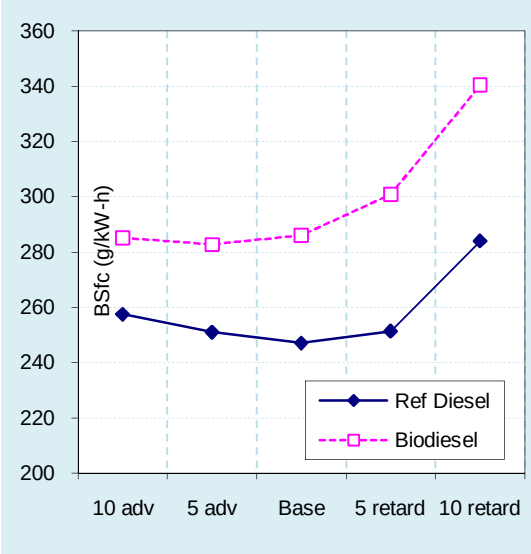

Fig.34 Brake specific fuel consumption for different injection timings

Figure 34 shows the brake specific fuel consumption (bsfc) as a function of injection timing. bsfc indicates the fuel economy of an engine at specific operating condition. Usually bsfc is minimized at MBT (maximum brake torque) timing, and if injection timing is retarded or advanced to MBT timing the bsfc increase. The trend can be clearly found in the plot above.

Figure 35 shows the $ISNO_2$ (indicated specific nitrogen dioxide) with respect to injection timings for both biodiesel fueled and diesel fueled cases. In direct injection compression ignition engines, nitric oxides formation largely depends on how high the gas temperature (combustion temperature) is and how long the temperature maintains. As

described earlier, injection timing has significant effect on cylinder pressure and temperature. Retarded injection timings lead to much lower combustion temperature than those at advanced timings, and this explains why $ISNO_2$ goes down with retarded injection timings as shown in the plot.

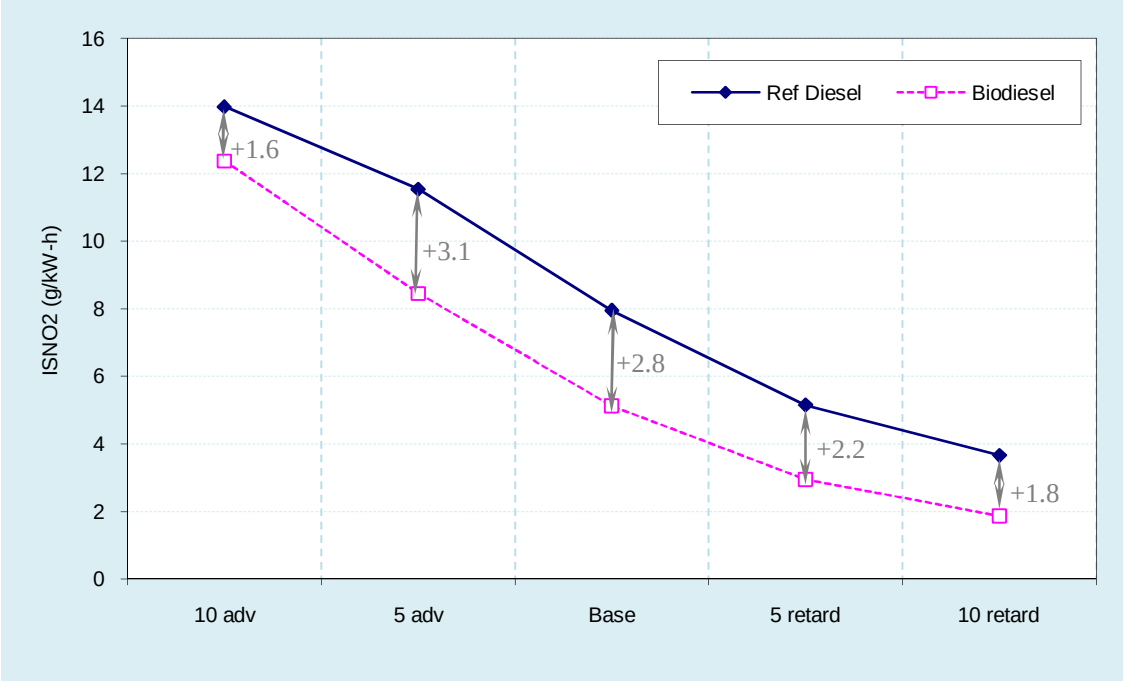

Fig.35 Indicated specific NO_2 for different injection timings

5.4.2 Injection pressure variation

As documented in the model description session, the injection pressure is a very important parameter which will significantly affect the fuel injection velocity and thereby penetration length and SMD (Sauter mean diameter). For the present study, injection pressure represents the peak injection pressure during the injection.

For diesel fueled case, change in pressure diagram with respect to five different injection pressures are plotted in the figure 36. As can be seen in the plot, higher injection pressure produces lower gas pressure in the cylinder, and vice versa. This can be explained by the fuel injection and mixing theory. Higher injection pressure produces

higher injection velocity, small SMD, and longer penetration length. These factors make the mixing process quicker which means the combustible air/fuel mixture is prepared more quickly, and finally ignition delay becomes shorter. In addition, shorter ignition delay will lower the gas temperature and pressure.

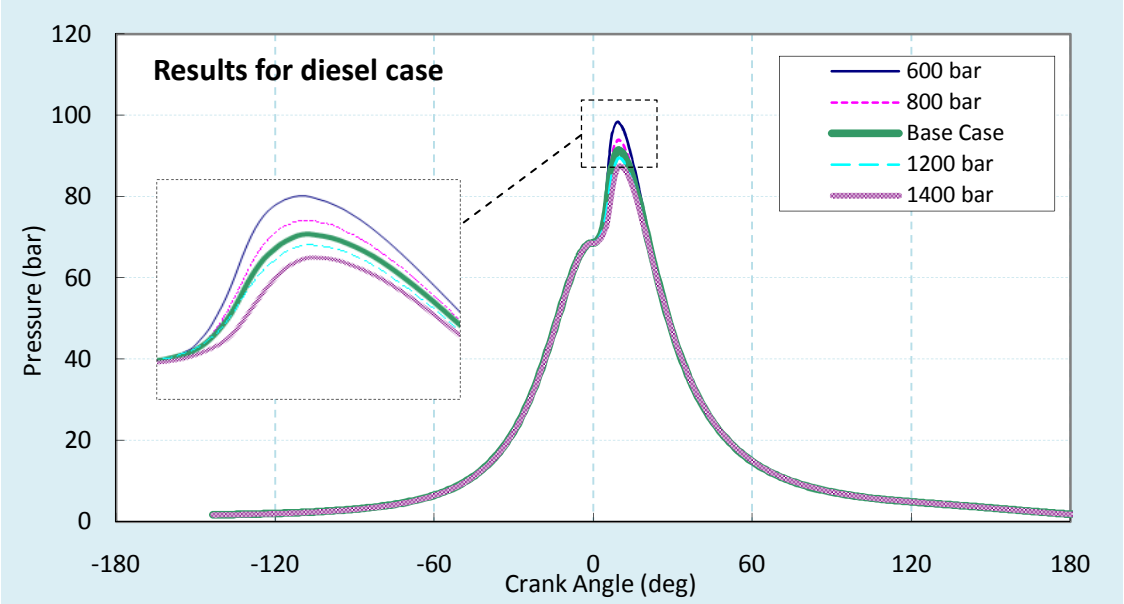

Fig.36 Pressure diagram for different injection pressure, diesel case

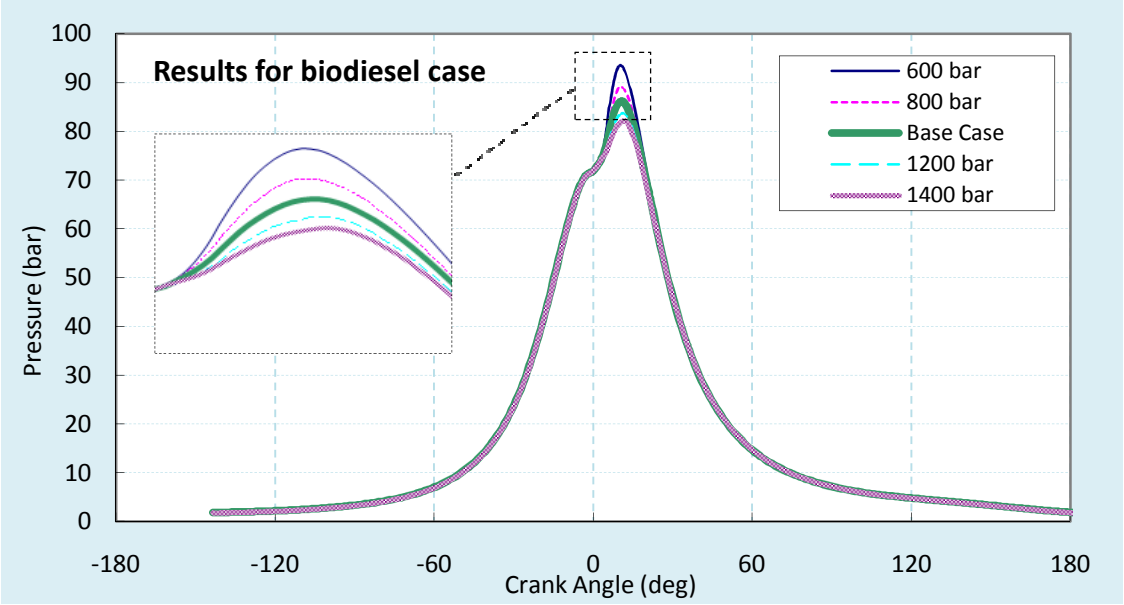

Fig.37 Pressure diagram for different injection pressure, biodiesel case

Very similar trends can be found for biodiesel fueled case as shown in figure 37. Figures 38 and 39 show the change in ignition delay and bsfc with respect to injection pressure, and trend has been discussed in the previous paragraph.

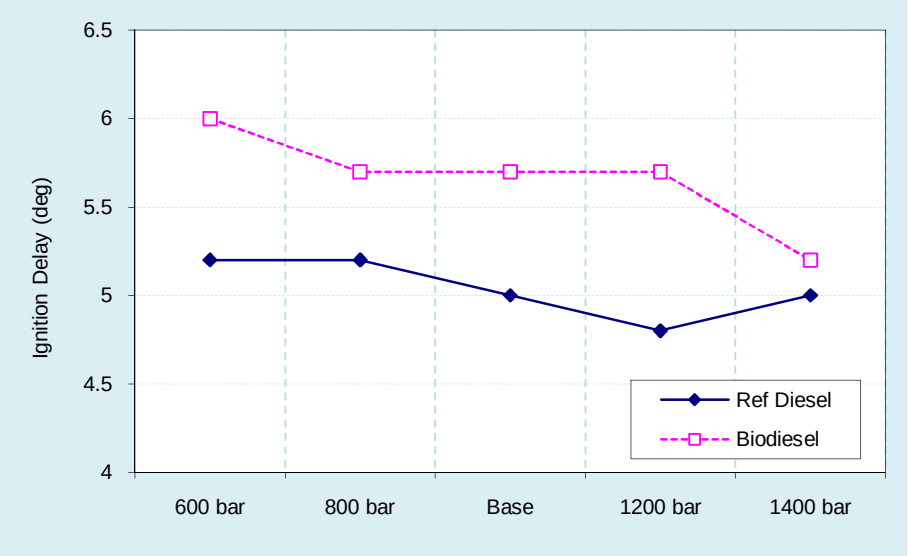

Fig.38 Ignition delay for different injection pressure

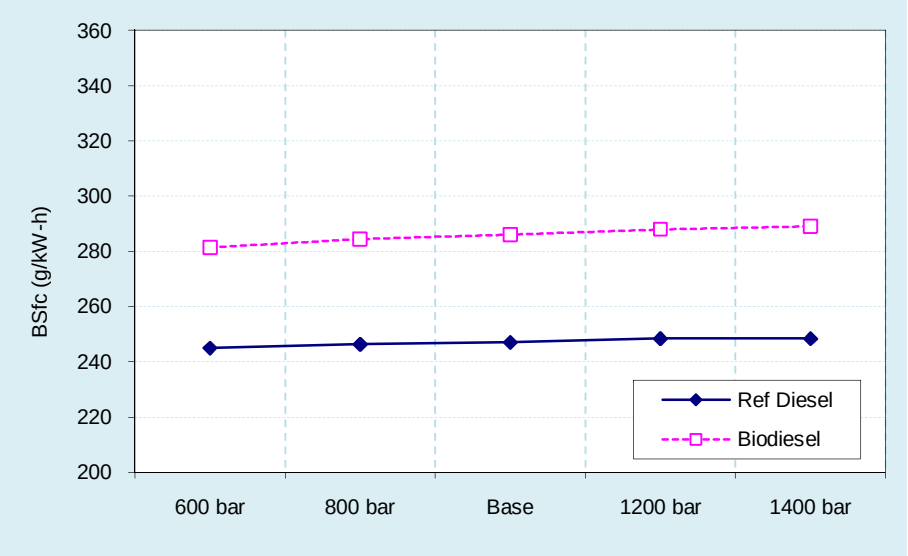

Fig.39 bsfc for different injection pressure

Figure 40 shows the $ISNO_2$ with respect to injection pressure. As documented before, higher injection pressure makes the combustion temperature lower, and combustion temperature is a key factor in nitric oxides formation. So, the $ISNO_2$ value decreases with the increase of injection pressure as seen in the plot. The trend is similar for both biodiesel case and reference diesel cases; and the diesel cases always produce higher $ISNO_2$ than the biodiesel case. More discussion on this topic is included in the next section regarding the emission formation.

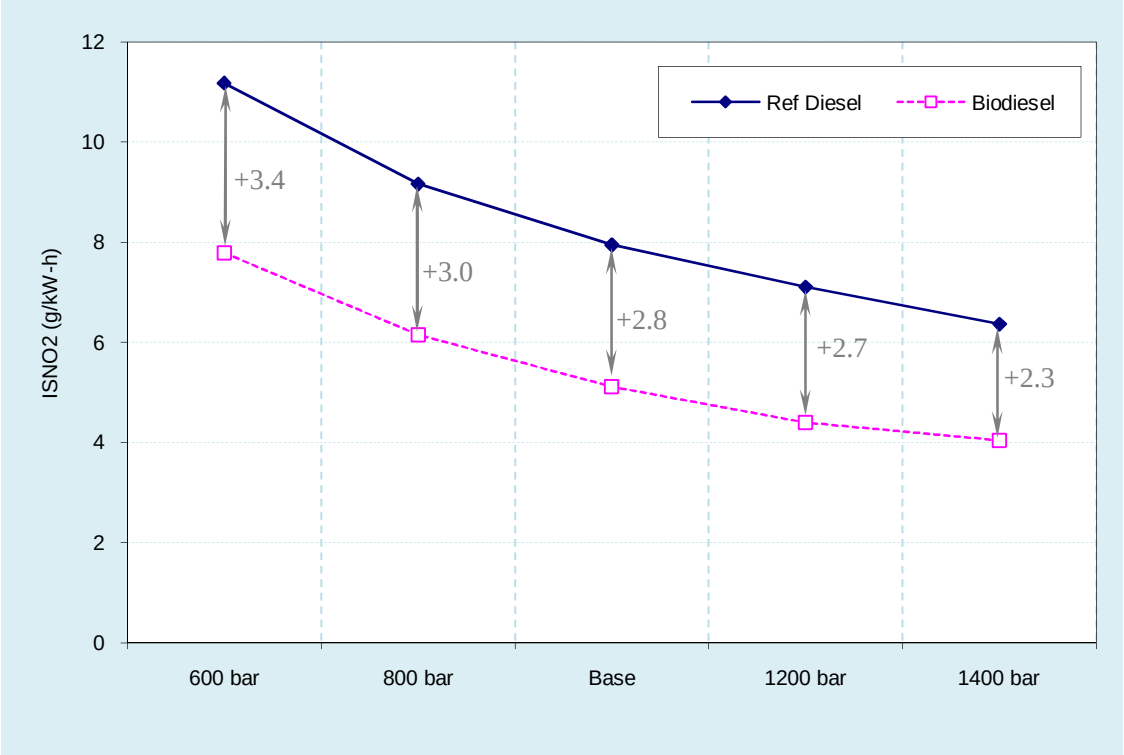

Fig.40 Indicated specific NO_2 for different injection pressure

5.4.3 Load/speed variation

The effect of engine speed on ignition delay at three different load conditions of 50 ft-lbs, 150 ft-lbs, and 300 ft-lbs for both diesel and biodiesel fueled case are plotted in figure 41. The ignition delay increases with the corresponding increase in speed as well as increase in load. In terms of absolute time of ignition delay rather than degree crank

angle, the ignition delay would decrease with increase of engine speed. That's because at higher engine speed, gas temperature and pressure is higher than those at lower engine speeds due to less heat loss. Therefore, the absolute ignition delay in units of seconds would be higher at higher engine speed. But on the other hand, at higher engine speeds, degrees crank angle in one second (may be described as deg/sec) increase more quickly than the decrease of ignition delay in seconds. So the combination of these two factors makes ignition delay in degree crank angle increase.

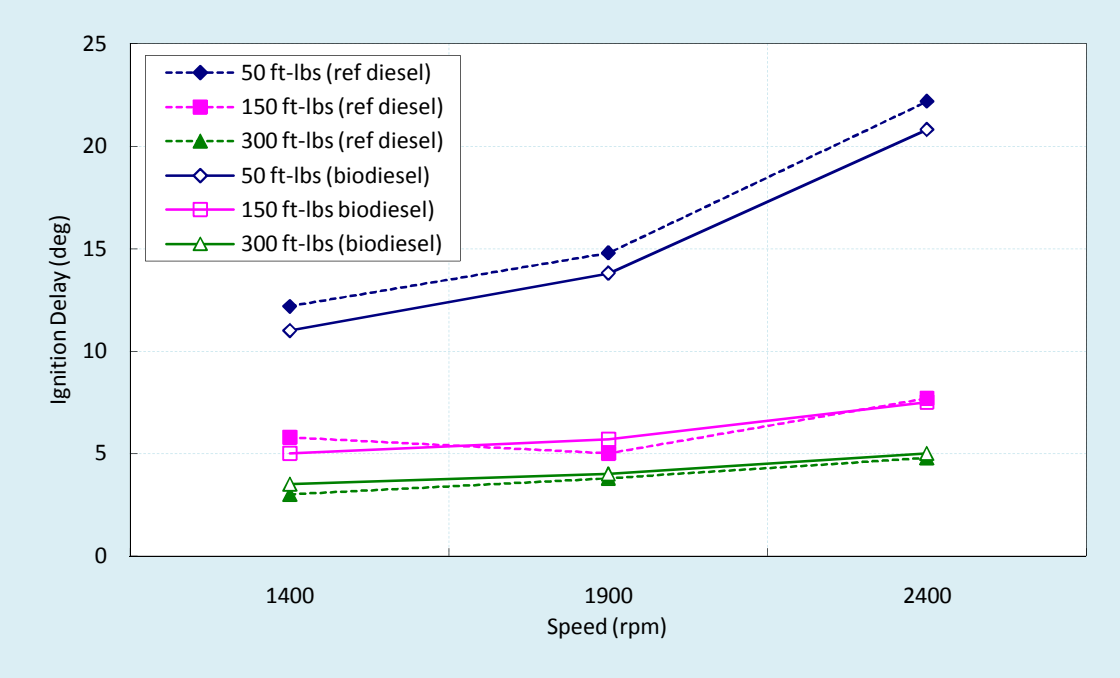

Fig.41 Ignition delay for different load and speed

Figure 42 shows bsfc as a function of speed for the three loads. At high and medium load conditions, the bsfc values are almost constant with speed. At low load conditions, bsfc is much larger than those at high and medium load conditions. The bsfc is reversely related to the thermal efficiency. From this point of view, the plot shows that medium and high load conditions thermal efficiencies are higher than those at low load conditions. This is because at low load conditions, exhaust energy is relatively low and therefore boost pressure is lower than those at higher load conditions; and the lower boost pressure leads to relatively lower thermal efficiency.

Figure 42 also compares the bsfc of biodiesel fueled cases and the diesel case. For at all nine operating conditions, the bsfc for the biodiesel cases are always higher than those for diesel case. This can be readily attributed to the lower LHV (lower heating value) of biodiesel. To produce the same torque as the diesel case, more biodiesel fuel is injected to the cylinder, which causes a higher bsfc of biodiesel fueled case.

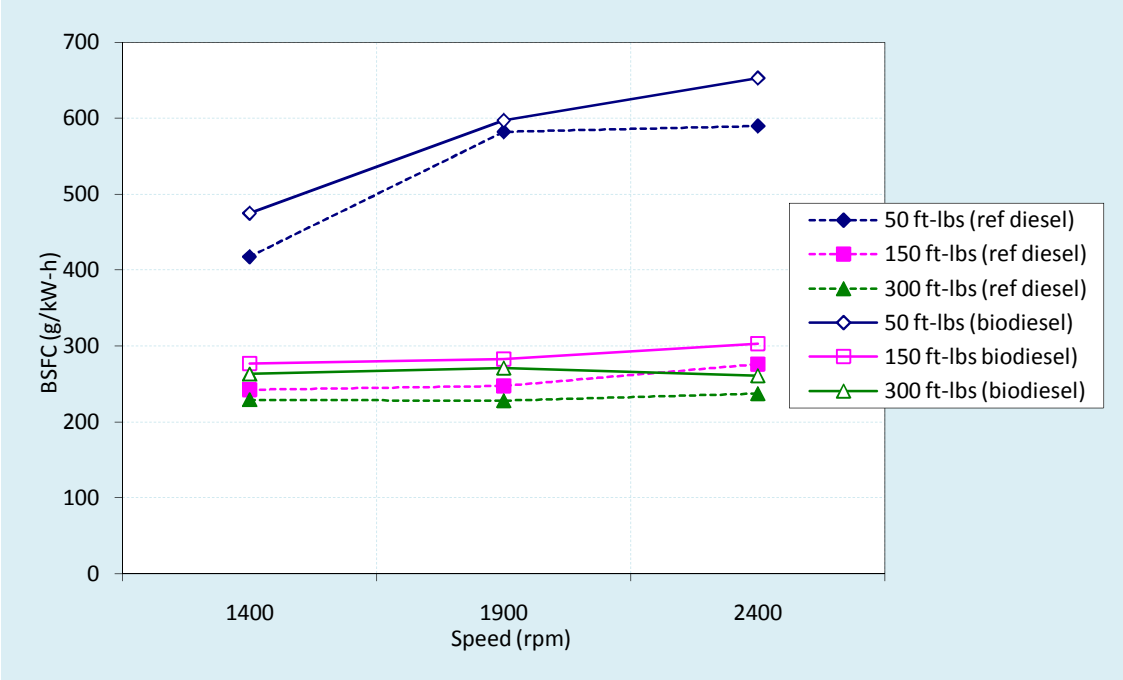

Fig.42 Brake specific fuel consumption for different load and speed

The EGR level applied at each operating conditions for diesel and biodiesel case are shown in figures 43 and 44. For both the diesel and biodiesel cases, no EGR is applied at low and medium load conditions, while 15%~25% EGR is used at high load conditions. According to the plots, large amount of EGR are used at 6 high load conditions (3 for diesel case and other 3 for biodiesel case), while at other conditions almost no EGR is applied.

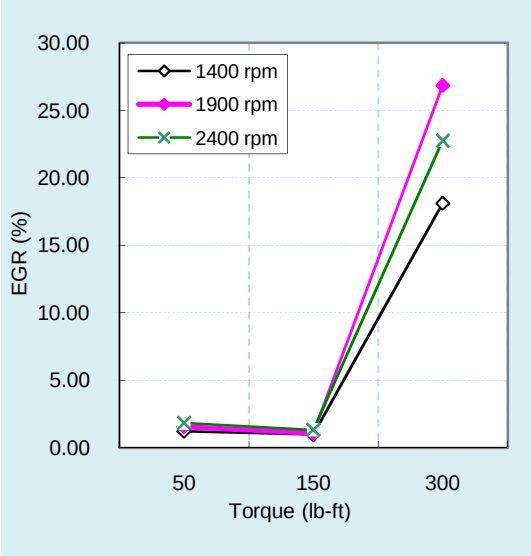

Fig.43 EGR level applied at each operating condition for reference diesel case

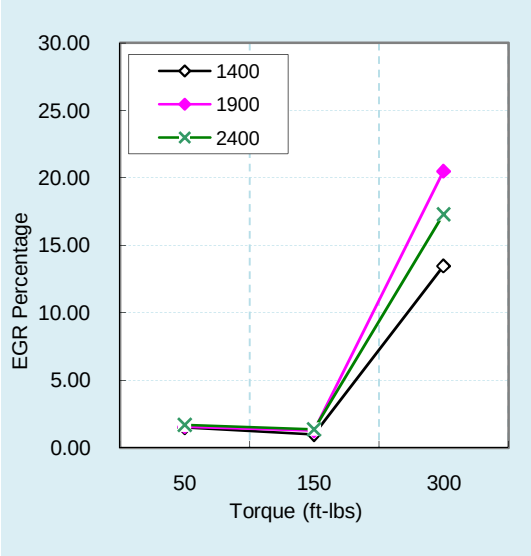

Fig.44 EGR level applied at each operating condition for biodiesel case

Figure 45 shows $ISNO_2$ as functions of engine speed for the three loads for diesel and biodiesel fuels. The $ISNO_2$ at medium load conditions are higher than those at low and high load conditions. In general, all cases using diesel fuel produced higher NOx than the biodiesel cases. Since the prediction of nitric oxides formation, even the measurement of NOx at current stage of this study are still very preliminary, the simulation results has a different trend with studies in most literatures, in which higher NOx emission for biodiesel case is found.

Since EGR are only applied at high load conditions, $ISNO_2$ values at 6 high load conditions (three for diesel cases and three for biodiesel cases) are typically lower than other cases due to EGR effect

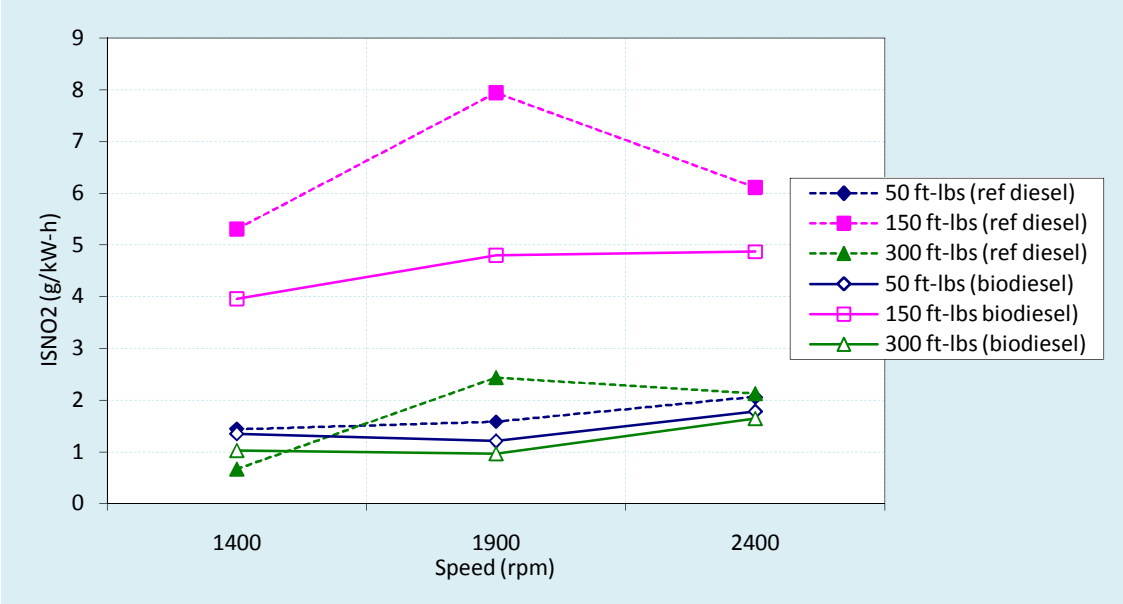

Fig.45 Indicated specific NO_2 for different load and speeds

5.4.4 EGR level variation

The effect of variation in EGR level on the cylinder pressures are shown in figures 46 and 47. The EGR levels do not have much effect on pressure trace, for both diesel and biodiesel case.

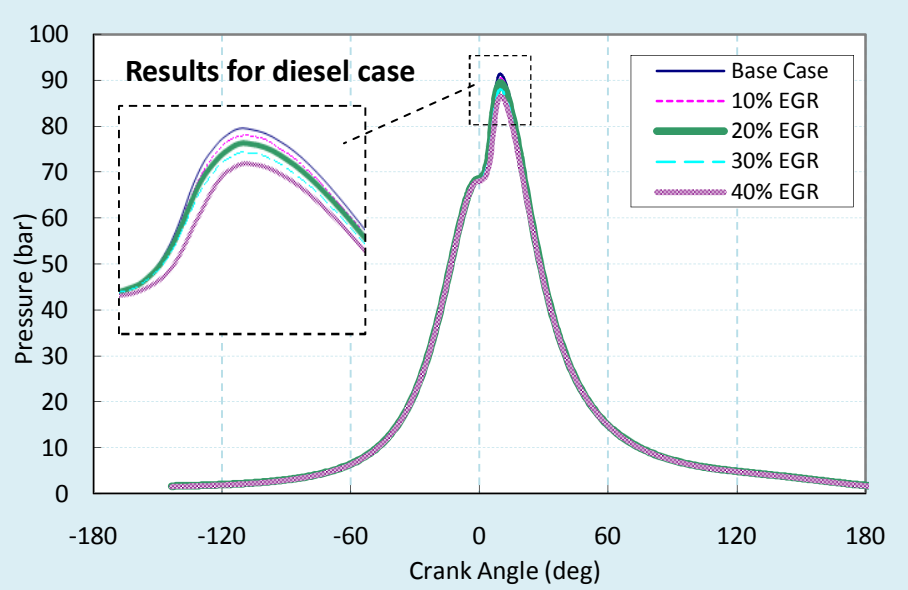

Fig.46 Pressure diagram for different EGR level, diesel case

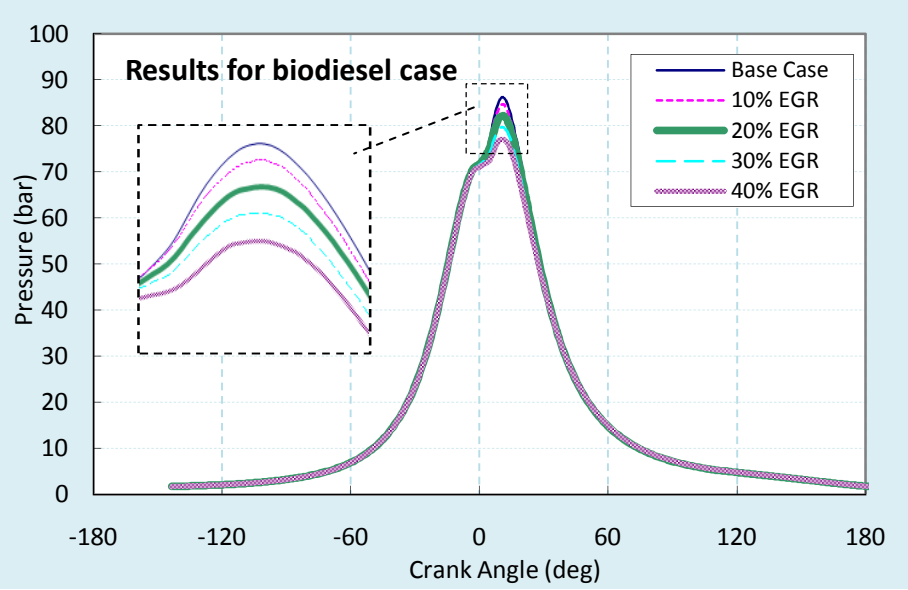

Fig.47 Pressure diagram for different EGR level, biodiesel case

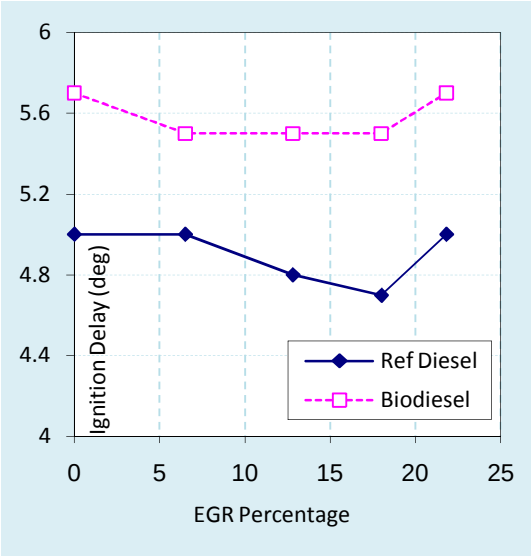

Fig.48 Ignition delay for different EGR level

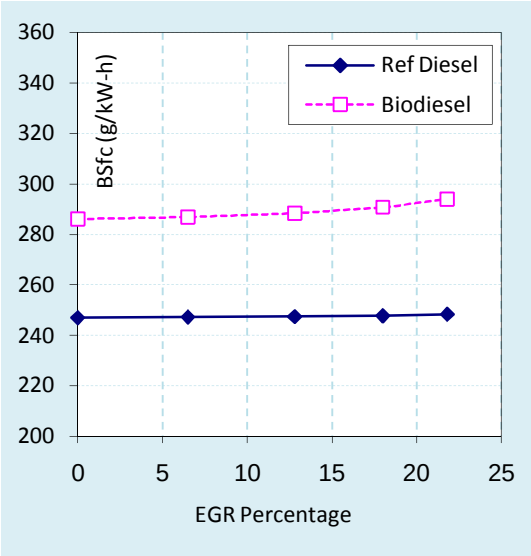

Fig.49 Brake specific fuel consumption for different EGR level

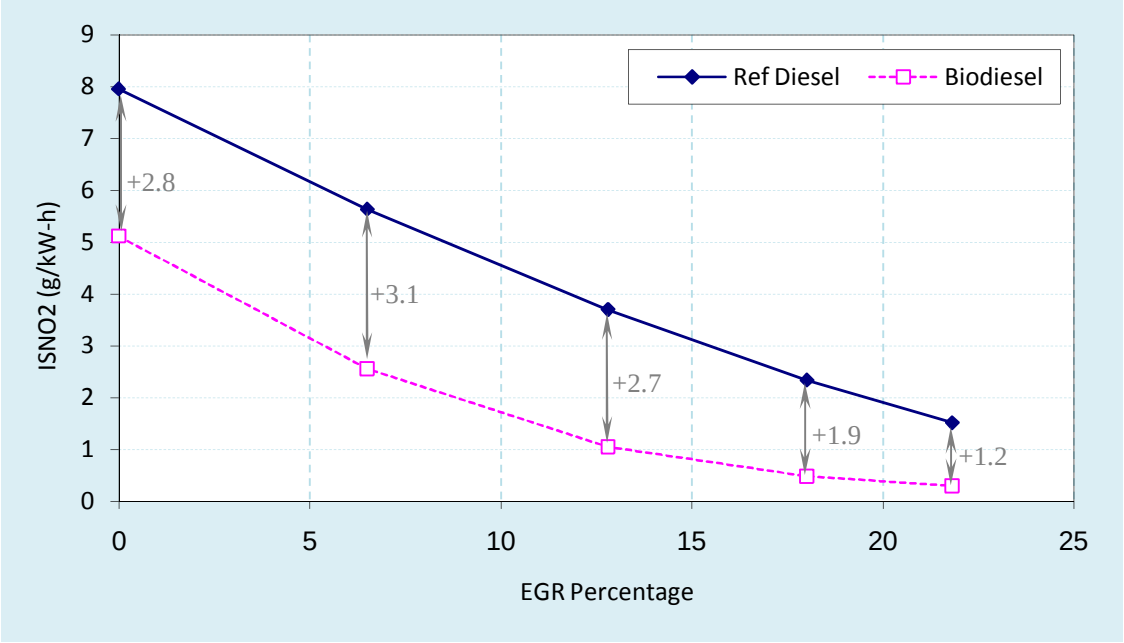

Fig.50 Indicated specific NO_2 for different EGR level

Figures 48 and 49 show the effect of EGR level on ignition delay and bsfc. Similar to the previous two plots, no significant effect caused by EGR level are noted. Hot EGR gases causes some difference in ignition delay but the effect is small. Similarly,

increasing EGR level leads to slightly increase of bsfc. Figure 50 shows effect of EGR level on NOx. As known by all, EGR is designed to depress the formation of NOx. This can be seen in the plot for diesel and biodiesel case.

5.4.5 Compression ratio variation

The parametric study for compression ratio variation is more conceptual than the above ones, since for a real engine, compression ratio of the engine is fixed unless there is a variable compression ratio feature.

Figures 51 and 52 show the effect of compression ratio on the cylinder pressures for diesel and biodiesel cases. Clearly, the pressures increase with the increase of compression ratio. This can be easily attributed to the ideal gas law which states pressure is reversely proportional to volume. Very similar trend is found both in diesel and biodiesel case.

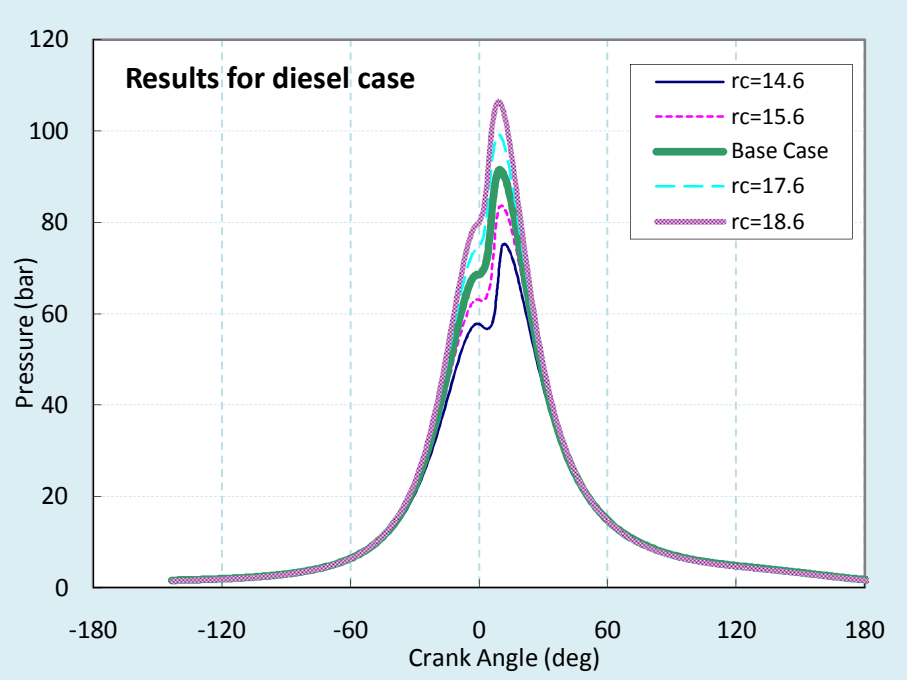

Fig.51 Pressure diagram for different compression ratio, diesel case

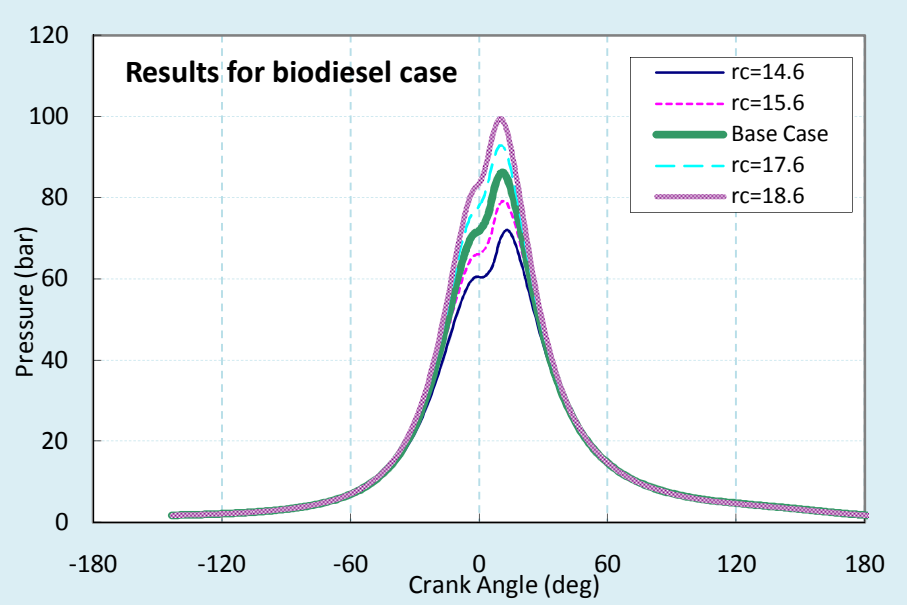

Fig.52 Pressure diagram for different compression ratio, biodiesel case

As documented earlier, higher compression ratio produces higher pressure and temperature by the end of compression. Then, the higher pressures and temperatures make the mixing of fuel and air more rapid and more combustible, and finally leads to low ignition delay. This is showed in figure 53.

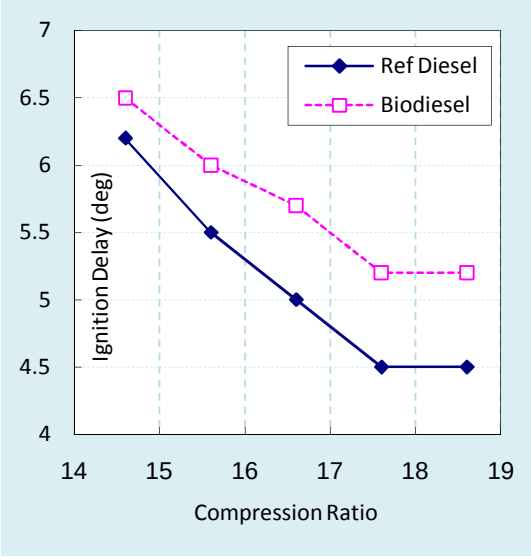

Fig.53 Ignition delay for different compression ratio

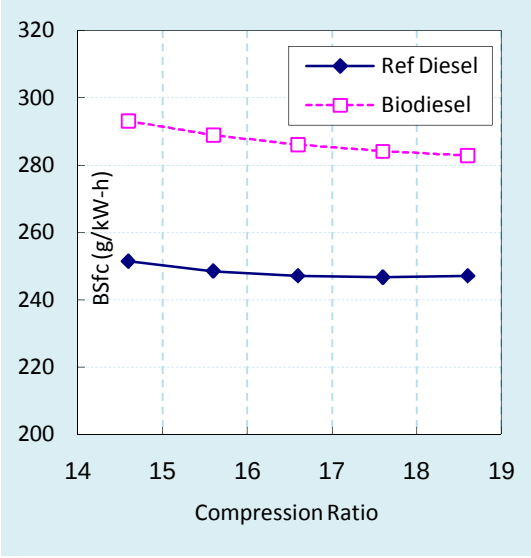

Fig.54 bsfc for different compression ratio

Figure 54 on the previous page shows the change in bsfc with respect to compression ratio. The increase of compression ratio produces higher pressure as shown previously which means higher power is generated with the same amount of fuel. Since bsfc is defined as fuel consumption divided by brake power, the bsfc decreases with the increase of compression ratio.

Effect of compression ratio on nitric oxides emission is also investigated, as shown in figure 55 higher gas temperature due to higher compression ratio is the main reason why $ISNO_2$ increases with the rise of compression ratio.

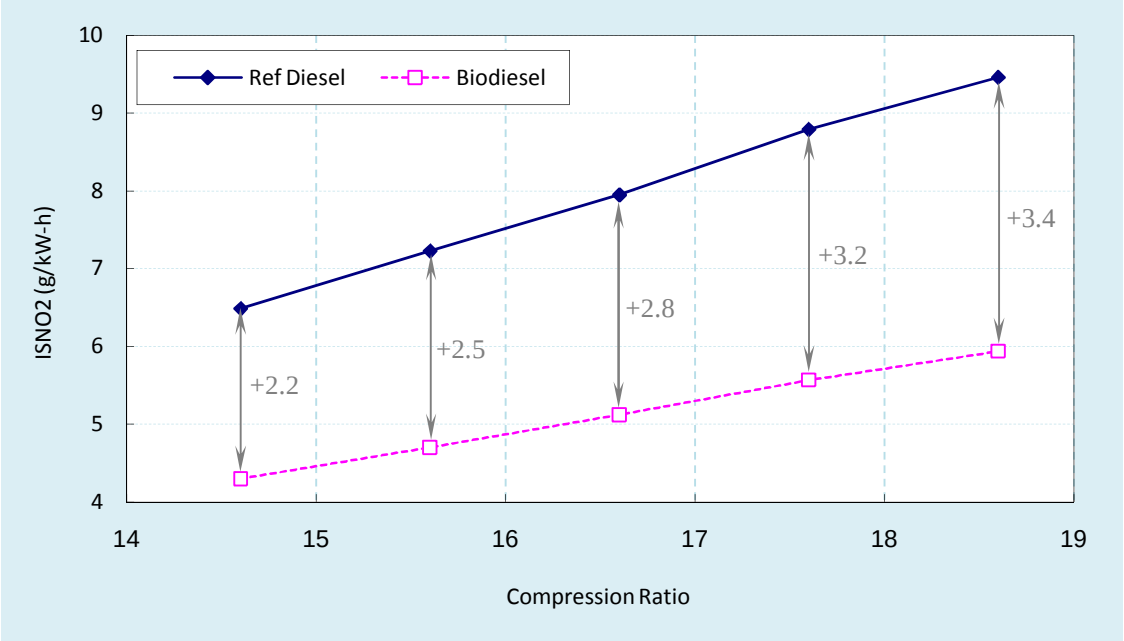

Fig.55 Indicated specific NO_2 for different compression ratio

5.5 Numerical study focusing on NOx emission

As documented earlier, biodiesel characteristically has lower particulate matter (PM) emissions, suggesting that characteristics of NOx emission from biodiesel would be very crucial for the use of biodiesel fueled direct injection compression ignition engines. In present study, though one-dimensional engine model cannot accurate predict the NOx emission, it would be very useful to study how individual mechanism or parameter affect nitric oxides emission.

5.5.1 Sensitivity of NOx prediction on major parameters

Based on a reference condition (1900 rpm 150 ft-lb), effect of change in several major parameters on NOx emission has been studied. The results are listed in the table 6 in the next page.

Among the six parameters that have been studied, radiation multiplier, wall temperature, and compression ratio are more conceptual ones. Radiation multiplier adjusts the amount of radiation heat transfer from high temperature gas in the cylinder to the cylinder wall. Less radiation heat transfer increases the NOx emission by 10 to 15 percent. This result is of interest because it is believed by some investigators that biodiesel combustion has less radiative heat transfer due to its lower PM emission. Similar to the radiation multiplier, wall temperature and compression ratio are also not very sensitive to NOx emission. These two parameters, to some extent, affect the gas temperature in the cylinder and finally affect the nitric oxides formation. In the above studied six parameters, both EGR level and injection timing has greatest effect on the NOx produced. A little adjustment could result in over 50% change in specific nitric oxides.

Table 6 How adjustable parameters affect the NOx calculation

Items	Change in $ISNO_2$ (g/kW-h)	
	Diesel	Biodiesel
Radiation Multiplier (from 1 to 0)	+ 13.8%	+ 15.6%
Radiation Multiplier (from 1 to 2)	-12.2%	- 14.3%
Start of Injection (5 deg advance)	+ 45.16%	+ 65.04%
Start of Injection (5 deg retard)	- 35.22%	- 42.58%
Injection Pressure (from 1000 bar to 800 bar)	+ 15.35%	+ 20.22%
Injection Pressure (from 1000 bar to 1200 bar)	- 10.57%	- 14.06%
Wall Temperature (from 450 K to 400 K)	-11.1%	- 12.0%
Wall Temperature (from 450 K to 500 K)	+ 12.1%	+ 12.9%
Compression Ratio (from 16.6 to 15.6)	- 9.06%	- 10.57%
Compression Ratio (from 16.6 to 17.6)	+ 8.20%	+ 8.79%
EGR Level (from 10% to 0%)	+ 41.21%	+ 100.00%
EGR Level (from 10% to 20%)	- 34.28%	- 58.98%

5.5.2 Numerical study of five NOx kinetics

As discussed earlier, in the present study the calculation of NOx is based on the extended Zeldovich mechanism which includes three NO formation reactions. The rate constant of each reaction, have been determined by many investigators **[24, 26, 27, 28, 29]**. Here five most widely-used kinetics (rate constants set) recommended by different investigators are applied to calculate NOx in the GT-Power simulation. The following table shows the details of each kinetics and its realization in GT-Power.

Table 7 The NOx kinetics studied and their realization in GT-Power

Kinetics				Realization in GT-Power		
	Number	Reaction	Rate Constant	F	A	Approximation
Heywood **[24]**	No.1	O+N2=NO+N	$7.6*10^{13}\exp(-38000/T)$	1	1	
	No.2	N+O2=NO+O	$6.4*10^{09}T\exp(-3150/T)$	1	1	
	No.3	N+OH=NO+H	$4.1*10^{13}$	1	N/A	
Baulch **[26]**	No.1	O+N2=NO+N	$7.6*10^{13}\exp(-38000/T)$	1	1	
	No.2	N+O2=NO+O	$6.4*10^{09}T\exp(-3150/T)$	1	1	
	No.3	N+OH=NO+H	N/A	0	N/A	
H&S **[27]**	No.1	O+N2=NO+N	$1.82*10^{14}\exp(-38350/T)$	2.39	1.01	
	No.2	N+O2=NO+O	$1.80*10^{10}T\exp(-4680/T)$	2.81	1.49	
	No.3	N+OH=NO+H	$1.10*10^{14}\exp(-1260/T)$	0.47	N/A	Yes
M&B **[28]**	No.1	O+N2=NO+N	$1.55*10^{13}T^{0.3}\exp(-37945/T)$	2.3	1	Yes
	No.2	N+O2=NO+O	$6.4*10^{09}T\exp(-3160/T)$	1	1	
	No.3	N+OH=NO+H	$3.8*10^{13}$	0.93	N/A	
D&B **[29]**	No.1	O+N2=NO+N	$1.95*10^{14}\exp(-38660/T)$	2.57	1.02	
	No.2	N+O2=NO+O	$9.0*10^{09}\exp(-3270/T)$	1.41	1.04	
	No.3	N+OH=NO+H	$1.10*10^{14}\exp(-565/T)$	0.62	N/A	Yes

Since the NO model in GT-Power offers only 5 adjustable rate constants in the kinetics, while some of the kinetics needs six of them, some approximation for H&S, M&B, and D&B kinetics are made, as shown in the figures 56 and 57. For the first rate constant of M&B kinetics, an exponential function is used to approximate the product of a polynomial and an exponential function (figure 56). For the third rate constants of H&S and D&B kinetics, two constants are used to approximate the corresponding exponential functions.

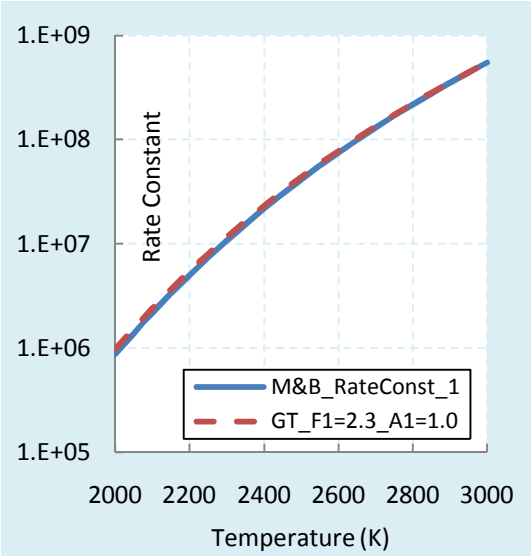

Fig.56 The approximation of M&B kinetics in GT-Power

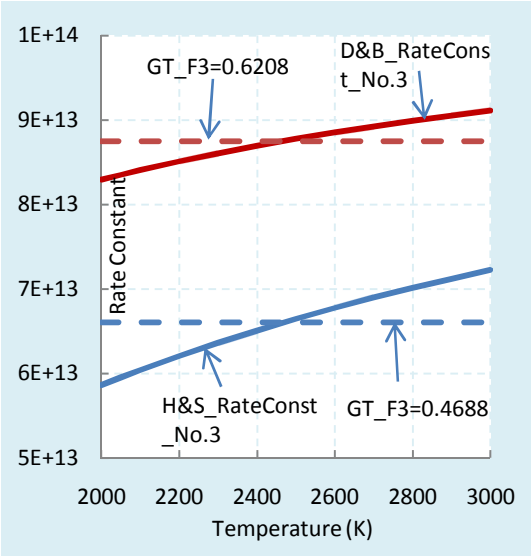

Fig.57 The approximations of H&B and D&B kinetics in GT-Power

Figure 58 shows the comparison between five nitric oxides kinetics for the reference diesel case at the base case described earlier. It clearly shows that the shape of NO concentration history in the cylinder are very similar to each other for different kinetics. Among the five kinetics, “M&B” predicted the highest “frozen concentration” of NO, while “Baulch” gave the lowest NO concentration.

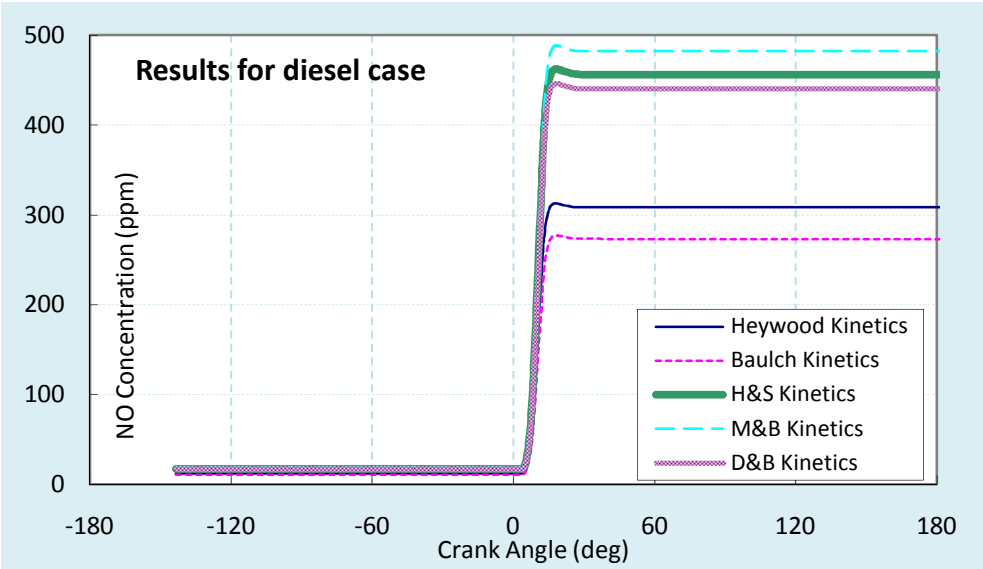

Fig.58 Comparison of NO calculation with different NO kinetics, diesel case

For the biodiesel case in figure 59, very similar results were obtained for the same five NO kinetics. The study of nitric kinetics indicates that at same operating conditions, different kinetics which means different rate constants could results in large difference in NO calculation. The highest value calculated by M&B kinetics is almost twice as the value calculated by Baulch kinetics.

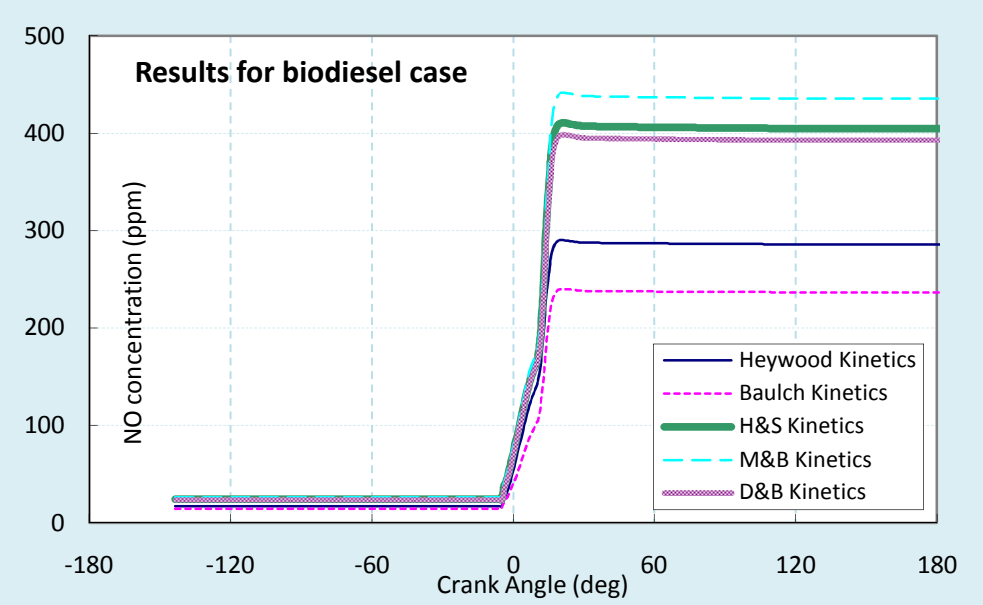

Fig.59 Comparison of NO calculation with different NO kinetics, biodiesel case

6. CONCLUSIONS AND RECOMMENDATIONS

A quasi-dimensional, multi-zone engine model of a four stroke compression-ignition engine was developed and applied to study the engine performance and emission characteristics with both reference diesel fuel and biodiesel fuel. At nine typical operating conditions, the engine model was calibrated for both diesel and biodiesel fuels. Pressure diagram and heat release curves at these operating conditions were compared between simulation and experiments. In addition, variations in pressure trace, ignition delay, brake specific fuel consumption, indicated specific nitrogen dioxide with respect to injection timing, injection pressure, load and speed, compression ratio, and percentage of exhaust gas recirculation were determined from both simulations with diesel and biodiesel fuel. Furthermore, focusing nitric oxides, the sensitivity studies and NO kinetics studies were made for both diesel and biodiesel case, and the results were compared between each other. Major results and conclusions can be summarized as follows:

1. The calibrated quasi-dimensional multi-zone model successfully predicted engine performance for both diesel and biodiesel fueled engine. Simulated pressure diagram and heat release curve at nine operating conditions showed good agreement with experimentally determined results.

2. Injection timing and compression ratio has the most significant effect on pressure diagram for both diesel and biodiesel fueled engine. Advanced injection timing and higher compression ratio leads to higher in-cylinder pressure, while retarded injection timing and small compression ratio lowers the pressure diagram. Comparing between diesel and biodiesel case, pressure diagram with biodiesel has lower peak pressure than that with reference diesel fuel for all the operating conditions and the parameters

considered for investigation. This observation might be attributed to the lower calorific value of biodiesel relative to diesel fuel.

3. The ignition delays for biodiesel fueled case were higher (3% ~ 10%) than the corresponding values for the diesel fueled case for medium load and high load conditions. In addition, variations in injection timing, injection pressure, and compression ratio would have certain effects (0.5~1.5 degree crank angle) on ignition delay for both biodiesel and diesel case.

4. The brake specific fuel consumption (bsfc) values for the biodiesel fueled engine were consistently higher (2%~12%) than the corresponding values for the diesel fueled case for all operating conditions and parameters studied. This results can be attributed to lower LHV of biodiesel. To achieve the same power output, more biodiesel fuel is required.

5. Results from sensitivity study shows injection timing and EGR percentage has the most significant effect on nitric oxides calculation (50%~100%) among the six parameters that is studied. In addition, changes in most of the parameters has greater effect on biodiesel fueled engine than the corresponding effect on diesel case. The NO kinetics study indicates that at the same base case, M&B kinetics predicted highest NO value while Baulch kinetics gave the lowest value.

Due to the unknown characteristics of the biodiesel fuel, some observations from both the simulation and the experiment still cannot be well explained. With more accurate experimental data, recommendations for future work are,

1. Calibrate the model to match the emission data from experiment, especially the nitric oxides emission. Together with burned zone temperature profile, compare the results with diesel and biodiesel fueled engine and find out the cause of the difference if there is any.

2. After getting the map for rack position of the VGT, include the compressor and turbine in the simulation rather than using compressor-out condition and turbine-in condition as inputs.

3. To get better understanding of biodiesel combustion in the cylinder, it would be useful to integrate the 3D computational fluid mechanics and detailed chemical kinetics into the current one-dimensional engine model. The simulation of intake/exhaust system could still be one-dimensional and the combustion in the cylinder could be simulated by 3D CFD and detailed chemical kinetics.

REFERENCES

1 US Department of Energy, Energy Information Administration, Available: http://www.eia.doe.gov/emeu/aer/pdf/pages/sec1.pdf, Accessed: 01/08/2009.

2 **Smaling, R.** Biodiesel and air quality: HARC Brownbag Presentation, Available: files.harc.edu/Documents/Announcements/2006/BiodieselAndAirQuality.pdf, Accessed: 03/22/2009.

3 **Monyem, A., Van Gerpen, J. H.,** and **Canakci, M.** The effect of timing and oxidation on emissions from biodiesel--fueled engines. *Trans. of the ASAE*, 2001, **44** (1), 35–42.

4 **Tat, M. E., Van Gerpen, J. H.,** and **Wang, P. S.** Fuel property effects on injection timing, ignition timing, and oxides of nitrogen emissions from biodiesel--fueled engines. *Transactions of the ASAE*, 2007, **50** (4), 1123-1128.

5 **Lu, X. M., Ge, Y. S., Wu, S. J.,** and **Han, X. K.** An experimental investigation on combustion and emissions characteristics of turbocharged DI engines fueled with blends of biodiesel. SAE paper 2005-01-2199, 2005.

6 **Yuan, W. Q., Hansen, C. A.,** and **Zhang, Q.** Computational modeling of NOx emissions from biodiesel combustion. *International Journal of Vehicle Design*, 2007, **45** (1/2), 12-32.

7 **Szybist, P. J., Kirby, R. S.,** and **Boehman, L. A.** NOx emissions of alternative diesel fuels: a comparative analysis of biodiesel and FT diesel. *Energy & Fuels*, 2005, **19**, 1484-1492.

8 **Wayne, A. E.** Effects of methyl ester biodiesel blends on NOx emissions. SAE paper 2008-01-0078, 2008.

9 **Chang, Y. Z.,** and **Van Gerpen, J. H.** Fuel properties and engine performance for biodiesel prepared from modified feedstock. SAE paper 971684, 1997.

10 **Senatore, A., Cardone, M., Rocco, V.,** and **Prati, V. M.** A comparative analysis of combustion process in DI diesel engine fueled with biodiesel and diesel fuel. SAE paper 2000-01-0691, 2000.

11 **Parvate-Patil, G., Vasquez, M.,** and **Payne, M.** Effects of Different Biodiesel Blends on Heat Release and its Related Parameters. ASME Internal Combustion Engine Division 2006 Fall Technical Conference, November 5-8, 2006, Sacramento, California, USA.

12 **Kinoshita, E., Myo, T., Hamasaki, K., Tajima, H.,** and **Zhang, R. K.** Diesel combustion characteristics of coconut oil and palm oil biodiesels. SAE paper 2006-01-3251, 2006.

13 **Ban-Weiss, G. A., Chen, J. Y., Buchholz, B. A.,** and **Dibble, R. W.** A numerical investigation into the anomalous slight NOx increase when burning biodiesel, a new theory. *Fuel Processing Technology*, 2007, **88**(7), 659-667.

14 **Agarwal, A.** Biofuels (alcohols and biodiesel) applications as fuels for internal combustion engines. *Progress in Energy and Combustion Science*, 2007, **33**, 233–271.

15 **Musculus, M.** Measurements of the influence of soot radiation on in-cylinder temperatures and exhaust NOx in a heavy-duty DI diesel engine. SAE paper 2005-01-0925, 2005.

16 **Yamane, K.** Influence of physical and chemical properties of biodiesel fuels on injection, combustin and exhaust emission characteristics in a direct injection compression ignition engine. *International Journal of Engine Research*, 2001, **2**(4), 249-261

17 **Jung, D.,** and **Assanis, D.** Multi-zone DI diesel spray combustion model for cycle simulation studies of engine performance and emissions. SAE paper 2001-01-1246, 2001.

18 **Arsie, I., Di Genova, F., Mogavero, A., Pianese, C.,** and **Rizzo, G.** Multi-zone predictive modeling of common rail multi-injection diesel engine. SAE paper 2006-01-1384, 2006.

19 **Kouremenos, D., Rakopoulos, C.,** and **Hountalas, D.** Multi-zone combustion modeling for the prediction of pollutants emissions and performance of DI diesel engines. SAE paper 970635, 1997.

20 **McCrady, J., Hansen, A.,** and **Lee, C.** Modeling biodiesel combustion using GT-Power. ASABE Meeting Presentation, Paper Number 076095.

21 GT-Power User Manual, Version 6.2, Gamma Technology, Inc, September 2006.

22 **Woschni, G.** A universally applicable equation for the instantaneous heat transfer coefficient in the internal combustion engine. *SAE Trans.*, 1967, **76**, 3065.

23 **Hohenberg, G.** Advanced approaches for heat transfer calculations. SAE paper 790825, 1979.

24 **Heywood, J.** *Internal Combustion Engine Fundamentals*, 1988 (McGraw-Hill, New York).

25 **Yoshizaki, T., Nishida, K.,** and **Hiroyasu, H.** Approach to low NOx and smoke emission engines by using phenomenological simulation. SAE Paper 930612, 1993.

26 **Baluch, D. L., Drysdale, D. D., Horne, D. G.,** and **Lloyd, A. C.** *Evaluated Kinetic Data for High Temperature Reactions, Vol. 2 – Homogeneous Gas Phase Reactions of the H2-N2-O2 System*, 1973 (Butterworths & Co. Ltd, London).

27 **Hanson, R. K.** and **Salimian, S.** Survey of Rate Constants in the N/H/O System, in Combustion Chemistry, ed. W. C. Gardiner, Jr., 1984 (Springer-Verlag, New York).

28 **Miller, J. A.** and **Bowman, C. T.** Mechanism and modeling of nitrogen chemistry in combustion. *Progress in Energy and Combustion Science*, 1989, **15**, 287-338.

29 **Dean, A. M.** and **Bozzelli, J. W.** Combustion Chemistry of Nitrogen, in Gas-Phase Combustion Chemistry, ed. W. C. Gardiner, Jr., 2000 (Springer-Verlag, New York).

APPENDIX I

PROPERTIES OF BIODIESEL AND DIESEL FUEL

Table 8 Properties comparison between diesel 2 and biodiesel

State	Item	Unit	Diesel No.2	Biodiesel
Vapor	C Atoms per Molecule		13.5	18.82
	H Atoms per Molecule		23.6	34.39
	O Atoms per Molecule		0	2
	N Atoms per Molecule		0	0
	Lower Heating Value	kJ/kg	43250	37150
	Critical Temperature	K	569.4	785.87
	Critical Pressure	bar	24.6	12.07
	Enthalpy	kJ/kg	See Table 9	See Table 9
	Viscosity	Pa-s	See Table 10	See Table 11
	Thermal Conductivity	W/m-K	See Table 10	See Table 11
Liquid	Heat of Vaporization	kJ/kg	250	357
	Density	kg/m^3	830	890.7
	Enthalpy	kJ/kg	See Table 12	See Table 12
	Viscosity	kg/m-s	See Table 13	See Table 14
	Thermal Conductivity	W/m-K	See Table 13	See Table 14

Table 9 Enthalpy constants for vapor diesel and biodiesel

Enthalpy Constants	Diesel No.2	Biodiesel
a1	1634.3	1675
a2	1.8191	1
a3	0	0
a4	0	0
a5	0	0

Note: The enthalpy of the vapor in J/kg is determined from the following curve-fit equation where h_{ref} is the enthalpy at the reference temperature, T_{ref}, of 298 K.

$$h - h_{ref} = a_1(T - T_{ref}) + a_2(T - T_{ref})^2 + a_3(T - T_{ref})^3 + a_4(T - T_{ref})^4 + a_5(T - T_{ref})^5$$

Table 10 Viscosities and thermal conductivities of diesel vapor

Temperature	Dynamic Viscosity	Thermal Conductivity
[K]	[Pa-s]	[W/m-K]
303.15	8.02e-006	0.00829904
373.55	6.75e-006	0.00829904
475.35	475.35	475.35

Table 11 Viscosities and thermal conductivities of biodiesel vapor

Temperature	Dynamic Viscosity	Thermal Conductivity
[K]	[Pa-s]	[W/m-K]
617	8.05715E-05	0.023996841
620	8.09543E-05	0.024174589
640	8.34962E-05	0.025364339
660	8.60214E-05	0.026562371

Table 11 Continued

680	8.85297E-05	0.027768685
700	9.10212E-05	0.02898328
720	9.34959E-05	0.030206157
740	9.59537E-05	0.031437315
760	9.83948E-05	0.032676755
780	0.000100819	0.033924477
800	0.000103226	0.03518048
820	0.000105617	0.036444765
840	0.000107991	0.037717331
860	0.000110348	0.038998179
880	0.000112688	0.040287309
900	0.000115011	0.04158472
920	0.000117318	0.042890413
940	0.000119608	0.044204387
960	0.000121881	0.045526643
980	0.000124137	0.046857181
1000	0.000126376	0.048196

Table 12 Enthalpy constants for liquid diesel and biodiesel

Enthalpy Constants	**Diesel No.2**	**Biodiesel**
a1	2050	2050
a2	0	0
a3	0	0

Note: The enthalpy of the liquid in J/kg at pressure=1 bar is determined from the following curve-fit equation,

where the reference enthalpy is defined as: $h_{ref} = (h_{ref})_{vapor} - h_{vaporization}$ and $T_{ref} = 298$ K

$$h - h_{ref} = a_1(T - T_{ref}) + a_2(T - T_{ref})^2 + a_3(T - T_{ref})^3$$

Table 13 Viscosities and thermal conductivities of liquid diesel

Temperature	Dynamic Viscosity	Thermal Conductivity
[K]	[Pa-s]	[W/m-K]
273.15	0.00219	0.116645
290.15	0.00171	0.113925
310.15	0.00133	0.110725
330.15	0.0011	0.107525
350.15	0.00096	0.104325
373.15	0.00088	0.100645
400.15	0.00087	0.096325
450.15	0.00112	0.088325

Table 14 Viscosities and thermal conductivities of liquid biodiesel

Temperature	Dynamic Viscosity	Thermal Conductivity
[K]	[Pa-s]	[W/m-K]
300	0.000045993	0.17887
310	0.000036646	0.17719
320	0.00002994	0.17549
330	0.000024982	0.17377
340	0.000021223	0.17205
350	0.000018309	0.17031
360	0.000016007	0.16855
370	0.000014157	0.16678
380	0.000012649	0.165
390	0.000011402	0.1632
400	0.00001036	0.16139
410	0.00000948	0.15955

Table 14 Continued

420	0.000008729	0.1577
430	0.000008083	0.15584
440	0.000007523	0.15395
450	0.000007034	0.15204
460	0.000006604	0.15011
470	0.000006224	0.14816
480	0.000005886	0.14618
490	0.000005584	0.14418
500	0.000005313	0.14216
510	0.000005069	0.14011
520	0.000004848	0.13803
530	0.000004647	0.13591
540	0.000004463	0.13377
550	0.000004296	0.13159
560	0.000004142	0.12937
570	0.000004	0.12711
580	0.000003869	0.12481
590	0.000003748	0.12247
600	0.000003636	0.12007
610	0.000003531	0.11762
620	0.000003434	0.11511
630	0.000003343	0.11253
640	0.000003259	0.10988

APPENDIX II

DISCHARGE COEFFICIENTS WITH LIFT

Table 15 Intake valve flow coefficients

L/D Ratio	Forward Flow Coefficient	Reverse Flow Coefficient
0	0	0
0.0304053	0.1071826	0.1071826
0.0608812	0.2031018	0.2031018
0.0911371	0.2788924	0.2788924
0.1215096	0.3513742	0.3513742
0.1519005	0.4214792	0.4214792
0.1823885	0.4814215	0.4814215
0.2128395	0.5291767	0.5291767
0.243119	0.5648113	0.5648113
0.2734641	0.5883421	0.5883421
0.3038992	0.6019374	0.6019374
0.3344928	0.6113458	0.6113458
0.3646257	0.6184707	0.6184707
0.3952485	0.6262355	0.6262355

Table 16 Exhaust valve flow coefficients

L/D Ratio	Forward Flow Coefficient	Reverse Flow Coefficient
0	0	0
0.0309989	0.1052954	0.1052954
0.0620698	0.2117053	0.2117053

Table 16 Continued

0.0929163	0.3008259	0.3008259
0.1238818	0.385439	0.385439
0.154866	0.4794244	0.4794244
0.1859492	0.5483239	0.5483239
0.2169947	0.5985104	0.5985104
0.2478653	0.6431867	0.6431867
0.2788029	0.6792136	0.6792136
0.3098321	0.7080437	0.7080437
0.341023	0.733009	0.733009
0.3717443	0.7526495	0.7526495
0.4029648	0.7682453	0.7682453

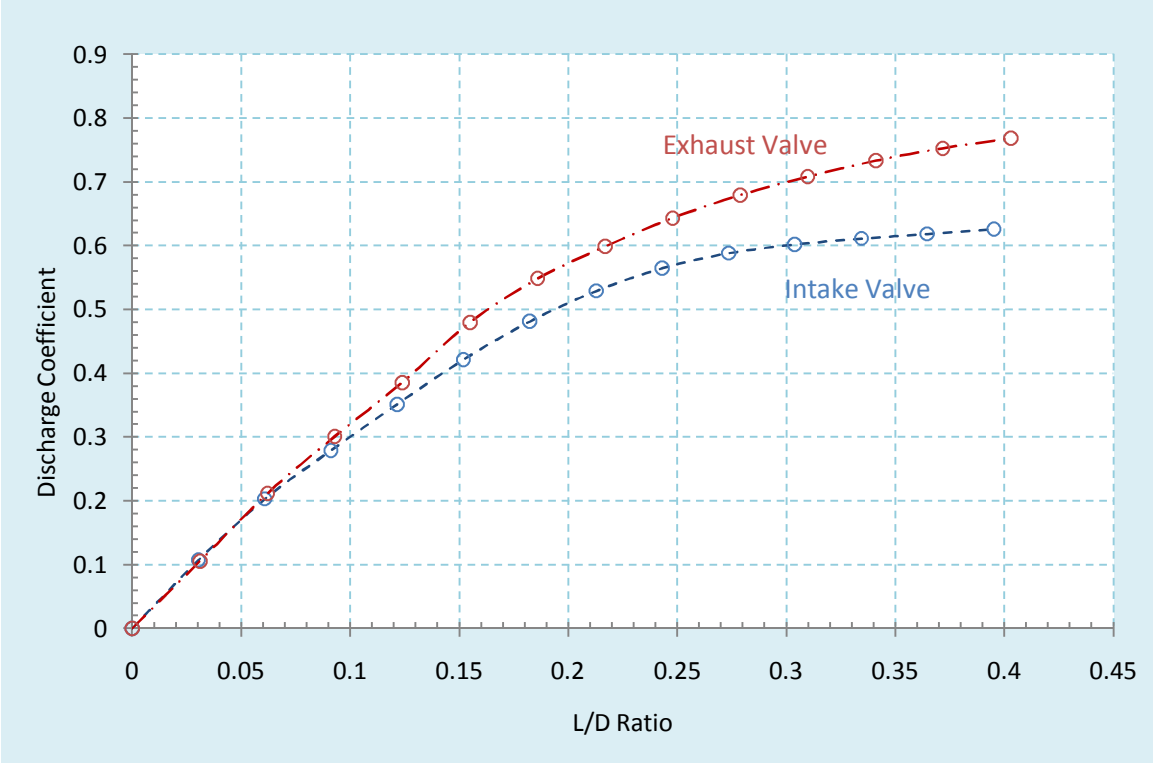

Fig.60 Discharge coefficients against L/D ratio for intake and exhaust valves

APPENDIX III

MODEL VALIDATION FOR BIODIESEL FUEL

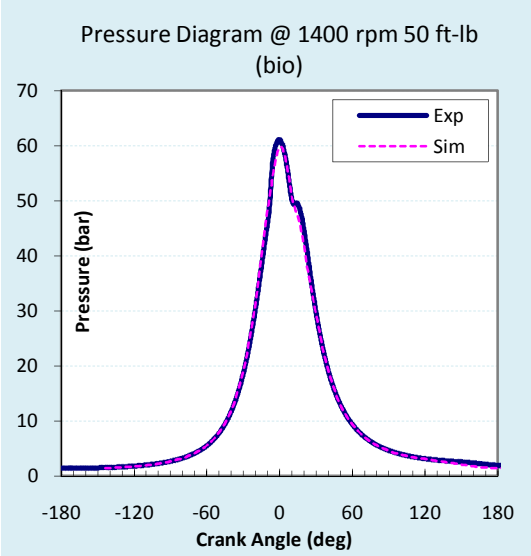

Fig.61 Pressure diagram comparison @ 1400 rpm 50 ft-lbs for biodiesel

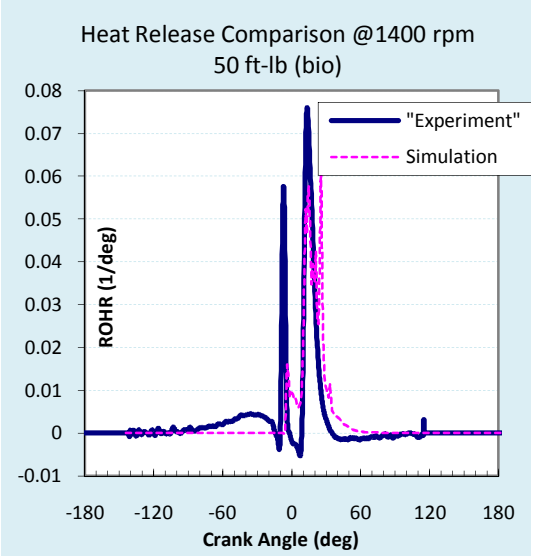

Fig.62 Heat release curve comparison @ 1400 rpm 50 ft-lbs for biodiesel

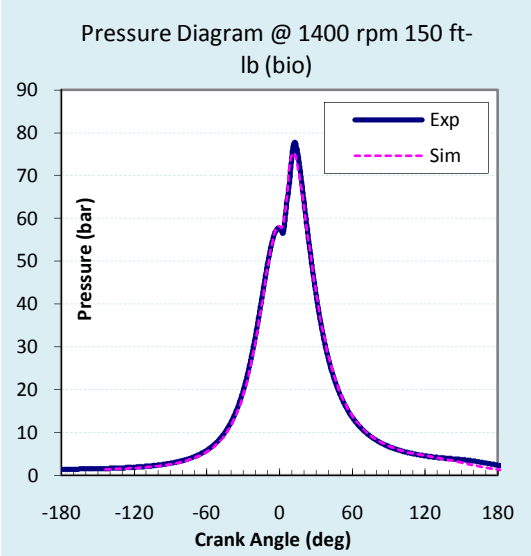

Fig.63 Pressure diagram comparison @ 1400 rpm 150 ft-lbs for biodiesel case

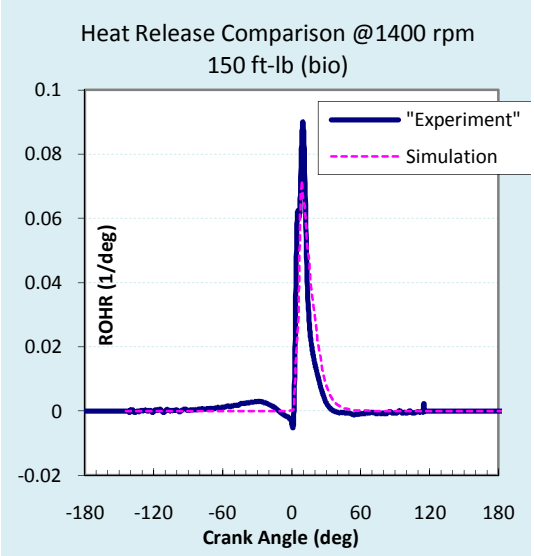

Fig.64 Heat release curve comparison @ 1400 rpm 150 ft-lbs for biodiesel case

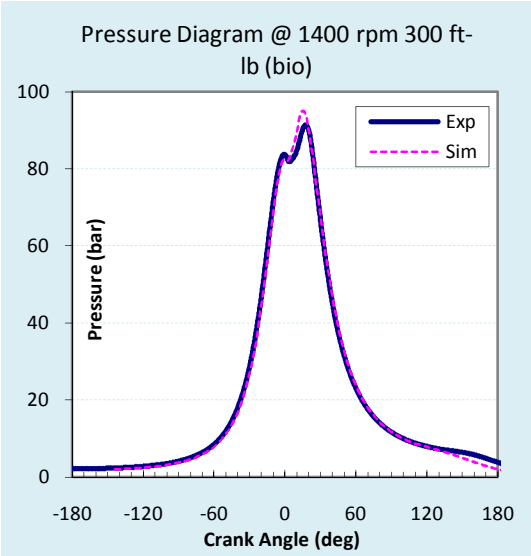

Fig.65 Pressure diagram comparison @ 1400 rpm 300 ft-lbs for biodiesel case

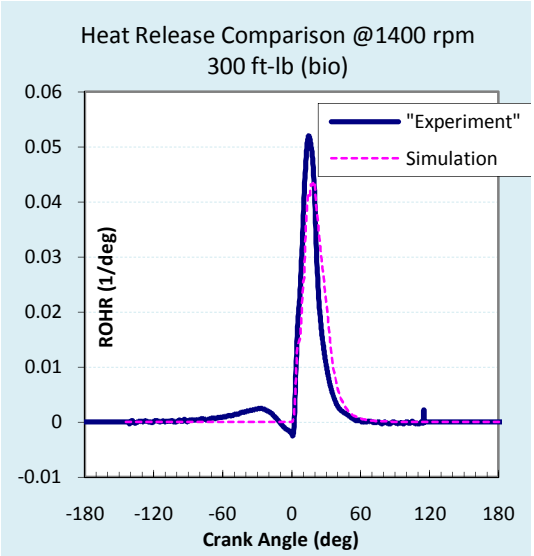

Fig.66 Heat release curve comparison @ 1400 rpm 300 ft-lbs for biodiesel case

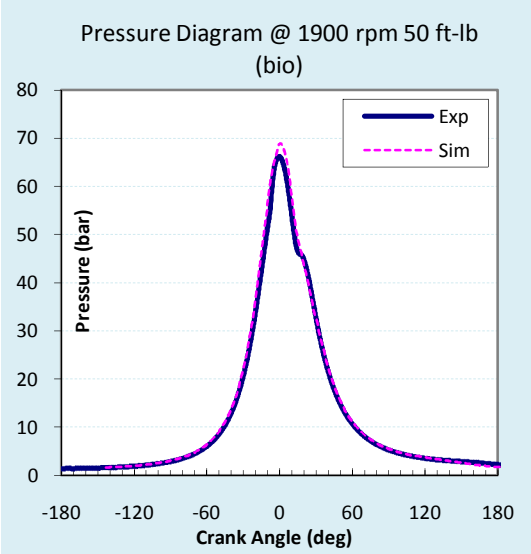

Fig.67 Pressure diagram comparison @ 1900 rpm 50 ft-lbs for biodiesel case

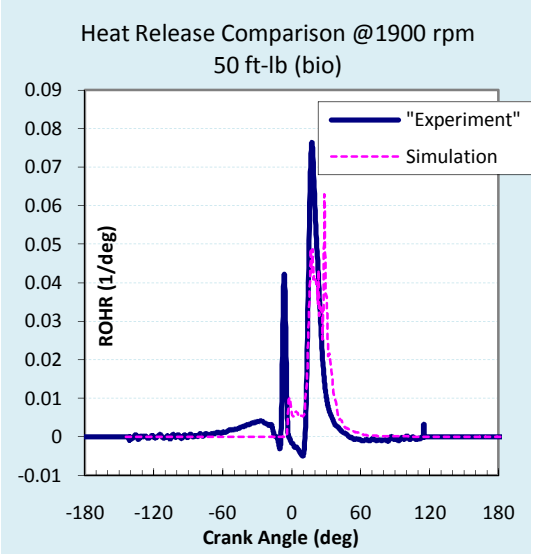

Fig.68 Heat release curve comparison @ 1900 rpm 50 ft-lbs for biodiesel case

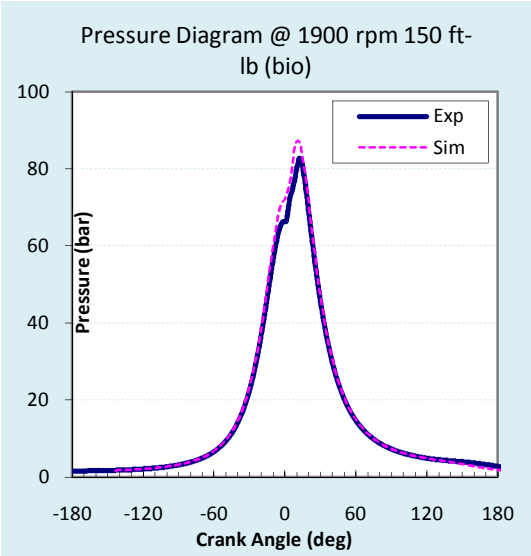

Fig.69 Pressure diagram comparison @ 1900 rpm 150 ft-lbs for biodiesel case

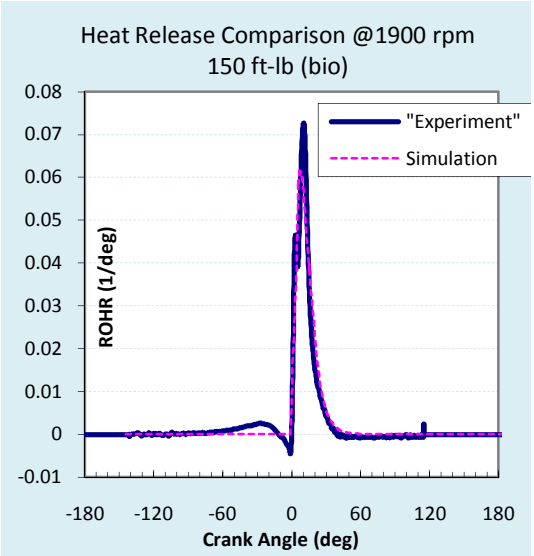

Fig.70 Heat release curve comparison @ 1900 rpm 150 ft-lbs for biodiesel case

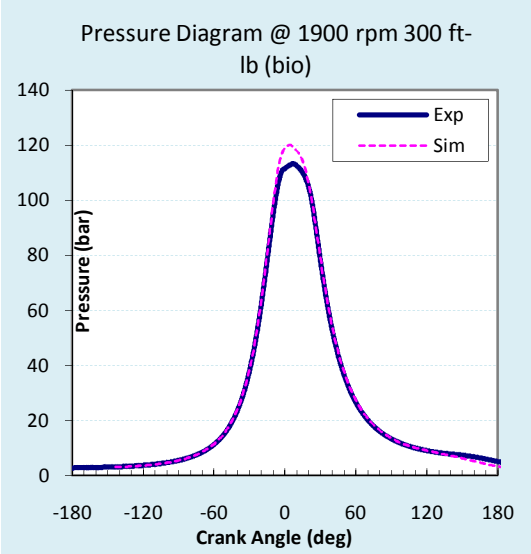

Fig.71 Pressure diagram comparison @ 1900 rpm 300 ft-lbs for biodiesel case

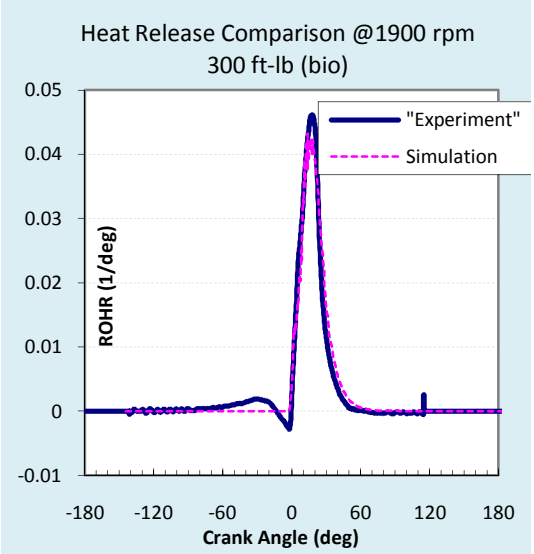

Fig.72 Heat release curve comparison @ 1900 rpm 300 ft-lbs for biodiesel case

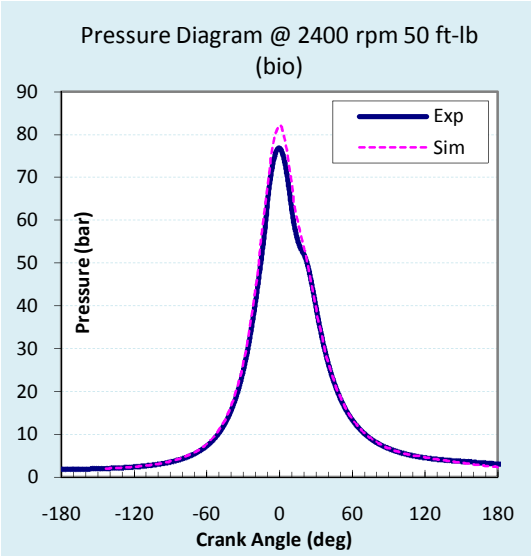

Fig.73 Pressure diagram comparison @ 2400 rpm 50 ft-lbs for biodiesel case

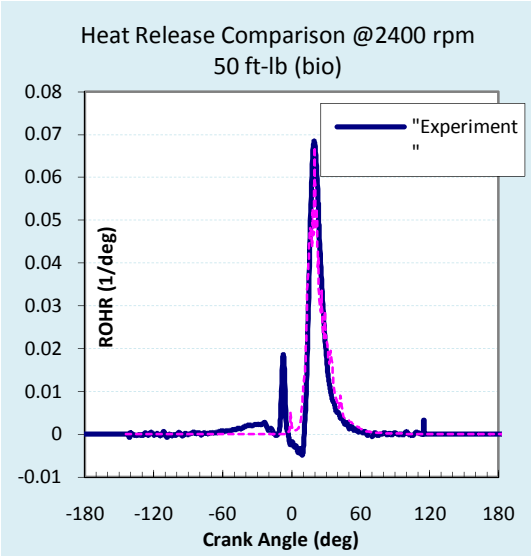

Fig.74 Heat release curve comparison @ 2400 rpm 50 ft-lbs for biodiesel case

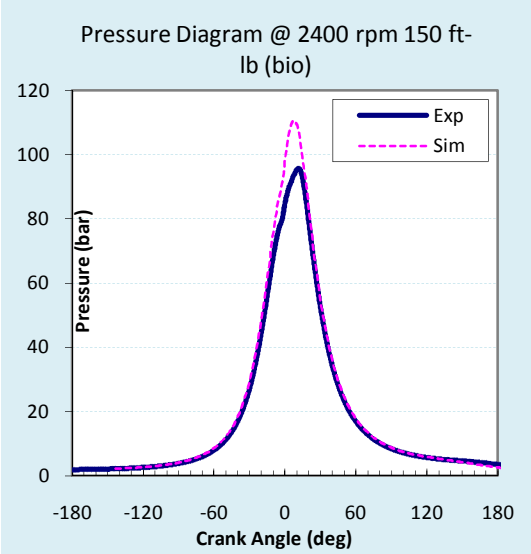

Fig.75 Pressure diagram comparison @ 2400 rpm 150 ft-lbs for biodiesel case

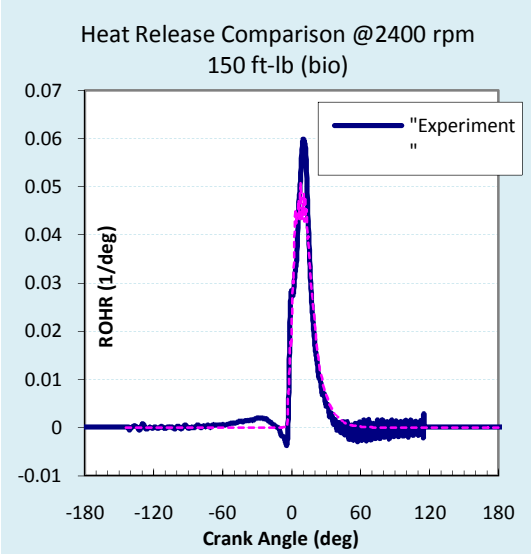

Fig.76 Heat release curve comparison @ 2400 rpm 150 ft-lbs for biodiesel case

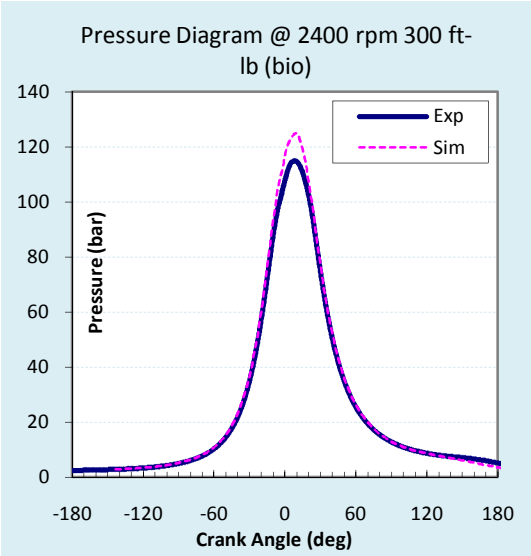

Fig.77 Pressure diagram comparison @ 2400 rpm 300 ft-lbs for biodiesel case

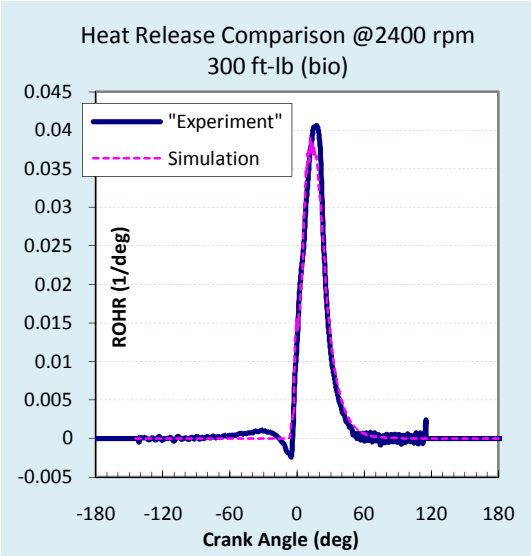

Fig.78 Heat release curve comparison @ 2400 rpm 300 ft-lbs for biodiesel case

VITA

Name:	Junnian Zheng
Address:	Texas A&M University Department of Mechanical Engineering 3123 TAMU College Station TX 77843-3123
Email Address:	zjn_flyer@neo.tamu.edu
Education:	B.A., Mechanical Engineering, Shanghai Jiaotong University, 2007 M.S., Mechanical Engineering, Texas A&M University, 2009